A Play of Light and Spins:

Excitation and Detection of Non-linear Magnetization Dynamics using Light

Shreyas Muralidhar

UNIVERSITY OF GOTHENBURG

Doctoral Dissertation in Physics

Department of Physics
University of Gothenburg
412 96 Gothenburg, Sweden

September 30, 2020

ISBN: 978-91-8009-006-3 (PRINT)
ISBN: 978-91-8009-007-0 (PDF)
URL: http://hdl.handle.net/2077/65625

Cover: Schematic of the unique pump probe experimental setup used in most part of this work. A red pulsed laser with 1 GHz repetition rate is used to pump the sample and a green continuous laser to probe the magnetization dynamics using Brillouin light scattering setup. The sample shown is a NiFe thin film with a protective coating of SiO_2, sputtered on sapphire substrate. (Image from *Editor's suggestion* section of Phys. Rev. B, **101**, 224423 (2020))

Printed by Stema AB, Borås, 2020
Typeset using LaTeX

"There are no mistakes. Only new paths to explore."

G. D. ROBERTS

Abstract

The excitation and detection of magnetization dynamics play key roles in the field of spintronics and magnonics. In this thesis, we investigate a contactless method of exciting nonlinear magnetization dynamics using a femtosecond pulsed laser, and study the same with a Brillouin Light Scattering (BLS) microscope. Further, we explore the synchronization characteristics of spin-Hall nano-oscillator (SHNO) arrays and their applicability to neuromorphics and Ising machines, using electrical measurement as well as optical measurements utilizing a phase-resolved BLS microscope.

After a brief introduction to the basic phenomena and techniques, the optical setup unique to this work is described in detail in Chapter 1. By using a frequency comb to pump the system, a strong enhancement of the weak scattering amplitude of the selected spin wave (SW) modes is observed. Additionally, the pump laser can be focused down to the diffraction limit and scanned along the focal plane to study the propagation characteristics of elementary excitations.

Frequency-comb-enhanced BLS microscopy was used to excite SWs in NiFe thin films (20 nm) and to study their characteristics. As the duration between consecutive pump pulses is shorter than the decay time of the magnons, sustained coherent emission of selected SW modes was observed. The BLS counts versus laser power follows a stronger than square dependence. This is in accordance with the Bloch $T^{3/2}$ law. The spatial map of the SW amplitude depicts strong unidirectional propagation of the main SW mode, whose direction of propagation can be controlled by changing the angle of the in-plane component of the applied field. An in-depth analysis of SW propagation at different fields showed a caustic X-pattern for high k-vector SWs, which has potential applications in the field of magnonics.

Chapter 3 lays the emphasis on two-dimensional SHNO arrays that show robust mutual synchronization up to arrays of 64 oscillators. Well-resolved BLS maps of the magnetization dynamics in the 2D arrays show that the oscillators in line with the direction of current synchronize first, which is followed by the four chains synchronizing together at higher currents. The applicability of 2D SHNO arrays in neuromorphics is demonstrated by injecting two external microwave signals, creating a synchronization map, like the one used for neuromorphic vowel recognition using vortex oscillators. Additionally, at higher powers of the injected signal, we demonstrate phase binarization of the microwave output using a phase-resolved BLS microscope. A direct application for solving combinatorial optimization (CO) problems using a SHNO array-based Ising machine is shown.

Contents

List of Figures

List of Symbols and Abbreviations

List of Symbols

α	Gilbert damping constant
H, H_{ext}	external magnetic field
I_{dc}	bias current
H_{eff}	effective magnetic field
H_A, H_k	anisotropy field
H_{int}	internal magnetic field
θ, θ_{ext}	external magnetic field angle
θ_{int}	out-of-plane angle of the magnetization
θ_{SH}	spin Hall angle
Ψ_{IP}	in-plane angle
M	magnetization
M_0, M_s	saturation magnetization
P	integrated power
ρ	resistivity
$\Delta f, \Delta H$	linewidth
f_{locked}	locked mode frequency
f_{FMR}	ferromagnetic resonance frequency
$\Delta\varphi$	phase difference
A_{ex}	exchange stiffness

List of Physical Constants

$\gamma/(2\pi)$	gyromagnetic ratio of an electron	$28.024\,\mathrm{GHz/T}$
μ_0	vacuum permeability	$4\pi \times 10^{-7}\,\mathrm{V\,s/(A\,m)}$
μ_B	Bohr magneton	$9.274 \times 10^{-24}\,\mathrm{J/T}$
e	elementary charge	$1.602 \times 10^{-19}\,\mathrm{C}$
$\hbar$	reduced Planck constant	$1.055 \times 10^{-34}\,\mathrm{J\,s}$

List of Abbreviations

AHE	anomalous Hall effect

List of Abbreviations (continued)

AMR	anisotropic magnetoresistance
BLS	Brillouin light scattering
CMOS	complementary metal-oxide semiconductor
dc	direct current
EBL	electron beam lithography
FMR	ferromagnetic resonance
FP	Fabry-Peròt
FWHM	full width at half maximum
GMR	giant magnetoresistance
HM	Heavy metal
HSQ	hydrogen silsesquioxane
IBE	ion beam etching
IP	in-plane
LLGS	Landau–Lifshitz–Gilbert–Slonczewski
LNA	low-noise amplifier
MR	magnetoresistance
MTJ	magnetic tunnel junction
OOP	out-of-plane
PSW	propagating spin wave
RBW	resolution bandwidth
RF	radio frequency
SEM	scanning electron microscope
SHA	spin Hall angle
SHE	spin Hall effect
SHNO	spin Hall nano-oscillator
STNO	spin torque nano-oscillator
STO	spin-torque oscillator
STT	spin transfer torque
SW	spin wave
TFPI	Tandem Fabry-Peròt Interferometer
TMR	tunneling magnetoresistance
TR-MOKE	time-resolved magneto-optic Kerr effect
VBW	video bandwidth
μ-BLS	microfocused Brillouin light scattering

Publications

List of papers and manuscripts included in this thesis:

I A. Aleman, **S. Muralidhar**, A. A. Awad, R. Khymyn, D. Hanstorp, and J. Åkerman "*Frequency comb enhanced Brillouin microscopy*", manuscript submitted to Optics Express.

Contributions: Fabrication of the samples, building the optical setup, measuring and data analysis. Contributed to writing the manuscript.

II **S. Muralidhar**, A. A. Awad, A. Aleman, R. Khymyn, M. Dvornik, D. Lu, D. Hanstorp, and J. Åkerman "*Sustained coherent spin wave emission using frequency combs*", Physical Review B **101**, 224423 (2020).

Contributions: Fabrication of the samples, building the optical setup, data acquisition and analysis and writing the manuscript.

III **S. Muralidhar**, R. Khymyn, A. A. Awad, A. Aleman, D. Hanstorp, and J. Åkerman "*Femtosecond laser pulse driven caustic spin wave beams*", arXiv:2006.08219, manuscript submitted to Physical Review Letters.

Contributions: Fabrication of the samples, designed the experiment, data acquisition and analysis and writing the manuscript.

IV M. Zahedinejad, **S. Muralidhar**, A. A. Awad, R. Khymyn, H. Fulara, H. Mazraati, M. Dvornik and J. Åkerman, "*Two-dimensional mutually synchronized spin Hall nano-oscillator arrays for neuromorphic computing*", Nature Nanotechnology **15**, 47 (2020).

Contributions: BLS measurements and electrical measurements and data analysis. Contributed to writing the manuscript.

V A. Houshang, M. Zahedinejad, **S. Muralidhar**, J. Chęciński, A. A. Awad, and J. Åkerman, "*A Spin Hall Ising Machine*", arXiv:2006.02236, manuscript submitted to Science.

Contributions: Phase-resolved BLS measurements and data analysis. Contributed to writing the manuscript.

Papers related to, but not included in this thesis:

1 H. Mazraati, **S. Muralidhar**, S. R. Etesami, M. Zahedinejad, S. A. Banuazizi, S. Chung, A. A. Awad, M. Dvornik and J. Åkerman, "*Mutual synchronization of constriction-based spin Hall nano-oscillators inweak*

in-plane fields", arXiv:1812.06350, manuscript submitted to Physical Review B.

2 H. Fulara, M. Zahedinejad, R. Khymyn, A. A. Awad, **S. Muralidhar**, M. Dvornik, and J. Åkerman "*Spin-orbit torque-driven propgating spin waves.*", Science Advances **5**, eaax8467 (2019).

Acknowledgments

Sometimes the journey is more beautiful than the destination. I couldn't have asked for a better experience than working with the wonderful researchers at Gothenburg University for the past four years. This work is an amalgamation of all the hard work, insightful discussions, constructive criticism, and successful collaboration with all the members of the group.

First and foremost, I would like to extend my heartfelt gratitude to Professor Johan Åkerman, who not only provided me with this opportunity, but also helped me along the scientific journey by encouraging me and guiding me through the process of development of skills that are valuable to a career in academics and in industry. His undying zeal and scientific curiosity motivated me to work on an entirely new research topic based on optics. His willingness to allow us to participate in many conferences helped me build my network in science. One of the most important skills that I developed over the four years of doctoral studies is to present well with clarity and confidence—and I owe it all to Johan.

I am very grateful to my co-supervisor, Dr. Ahmad Awad, for painstakingly mentoring me on a daily basis. The depth of his knowledge surprises me every time, and there is always something new to learn from him. I cherish all the hours spent in the lab building optics, brainstorming ideas, and discussing the results with him. His commitment to the project inspired me to work harder and to obtain fruitful results that have been incorporated in this thesis.

My special thanks go to all my colleagues from the group at Gothenburg University: Mohammad Zahedinejad, Afshin Houshang, Roman Khymyn, Mykola Dvornik, Himanshu Fulara, Martina Ahlberg, Sheng Jiang, Hamid Mazraati, Jinjin Yue, Randy Dumas, and Mohammad Haidar. Their active support has played a crucial role in making my life in Gothenburg a lot simpler. I could always count on them for any help I needed within the department—and outside it too.

Given my background in solid state physics, I admit that I had some trouble getting my head around optics in the beginning. So I am extremely thankful to Ademir Aléman, with whom I share the success of this project, for helping with the design of the optical layout, and for patiently explaining difficult topics in optics in a way I could grasp. I thoroughly enjoyed his company and I look forward to more years of collaboration.

I would like to extend my gratitude to my examiner, Professor Dag Hanstorp, for making the entire duration of my Ph.D. studies effortless. He also participated proactively in the project, and his rich experience in the field of optics was a key addition to the success story.

Apart from all the academic support I received, a great deal of help was provided by the administrative staff, for which I am very grateful. I would like to make special mention of Bea Tensfeldt, Maria Siirak, and Pernilla Larsson for taking the extra effort in handling all the bureaucratic procedures quite effortlessly. I am grateful to Mats Rostedt and Jan-Åke Winman for providing all the technical assistance needed to build the labs and keep them operational.

A balanced life is a happy life. I would like to thank all my friends in Gothenburg for bearing with me and giving me a wonderful time that I will cherish for the rest of my life. I am particularly thankful to Akhil Krishnan, Akhil Neelakanta, Manish, Prarthana, Namratha, Badhri, Anandh, Rakshith, Sujee, and Kovendhan for being there for me whenever I needed them.

Finally, my heartfelt gratitude goes to my parents for encouraging me and giving me the freedom to do what I love, and for bringing me up with endless love and care. I hope I have made them proud. This thesis is entirely dedicated to them, and to my brother for his practical insights about life, to my cousins for encouraging and caring about me boundlessly. Last but not least, I thank my guru Sri Sathya Sai Baba for showing me the path and guiding me through different walks of life, making me the human being that I am today. I cannot thank them all enough for their unconditional love and support.

Introduction

Light is a source of energy that can be utilized to excite materials, control physical processes, and study underlying phenomena. In magnetism, ultrafast demagnetization using laser pulses on the order of a few femtoseconds is the fastest known magnetization quenching process, the discovery of which opened up a new field of research called ultrafast magnetism. More than two decades have passed since the seminal experiment on nickel showing rapid demagnetization of the magnetic moment on a subpicosecond timescale [1], yet the underlying phenomena of ultrafast demagnetization have not been unraveled completely. Several groups have worked on the topic since then, on a range of magnetic materials [1–5]. Rapid quenching has led to several interesting phenomena, such as all-optical switching [6–10], emission of spin waves (SW) [3, 11–17], THz emissions [18–20], laser-induced spin-transfer torque (STT) [21], emission of super-diffusive spin currents [22–25], and laser-induced phase transformations [26, 27]. Each of these findings has led to interesting research areas with potential technological applications.

Spin waves (SWs) or magnons (the quanta of SWs) lie at the heart of magnonics. In contrast to conventional CMOS-based electronics operating at a few GHz, magnons can operate at several tens of GHz and have a shorter wavelength than their electromagnetic counterparts at a similar frequency, and have thus come to play an important role in the development of faster, smaller, and more energy efficient devices in this era where the internet of things (IoT) has become an integral part of human life. The generation, manipulation, and detection of SWs are key processes for implementing logic functions in magnonic devices[28–31]. SWs can be generated using microwave antennas [32–34] or STT-driven oscillations [35–43]. Alternatively, pulsed laser excitation is a contactless way of generating SWs in magnetic materials, and gives a notable advantage in terms of freedom to move the SW emission spot without changing the sample layout. To date, many groups have conducted single-pulse experiments [3, 11–14, 44–46], where the system returns to equilibrium before the arrival of a second pulse. Very few studies have attempted sustained coherent excitation of SWs [47–49] using high repetition-rate lasers [15, 16].

STT-driven oscillations in nanoscale spintronic devices have shown a multitude of non-linear magnetization dynamics, such as high-frequency oscillations [50, 51], propagating SWs [36, 37, 52, 53], SW bullets [35, 54–56], and magnetic droplets [57–60]. However, these devices suffer from certain disadvantages such as low output power and high phase noise. These drawbacks can be mitigated by synchronizing multiple oscillators. Although reading the microwave output electrically is both faster and more practical, optical study using BLS

microscopy ($\mu-$BLS) allows us to spatially map the magnetization dynamics. Spin-Hall nano-oscillators (SHNOs) are a class of STT-based oscillators that operate through high-density pure spin-currents being injected into a ferromagentic layer due to the spin-Hall effect in the adjacent heavy metal layer [61, 62]. The possibility of fabricating large ensembles of SHNOs, and the easy accessibility they offer for optical study makes them an interesting candidate. Robust mutual synchronization of a chain of nine SHNOs has already been shown [63]. The phenomenon of synchronization has been proven useful for several alternative non-von Neumann computing paradigms.

The goal of this thesis is to explore the generation and detection of nonlinear magnetization dynamics mainly using light. The thesis is hence focused on ***i.*** sustained coherent emission of spin waves using GHz frequency combs in NiFe thin films, and studying their characteristics and tunability using an integrated highly sensitve $\mu-$BLS setup with a six-pass tandem Fabry-Perot Interferometer (TFPI); and ***ii.*** Robust mutual synchronization of two-dimensional arrays of SHNOs, and their application in computing paradigms such as neuromorphics and Ising machines.

This thesis is organized as follows:

Chapter 1 introduces the basic physics that is vital to the understanding of concepts and results in the thesis. A description of sample fabrication and experimental techniques used in the thesis is given, including a detailed description of the optical setup unique to this work. The two optical systems—a femtosecond-pulsed pump system operating at a GHz repetition rate and a continuous wave probe system called a Brillouin Light Scattering (BLS) microscope—have been integrated.

Chapter 2 begins with the technical details of the integrated frequency-comb-enhanced BLS microscopy, which can be used in various fields of research. The scanning system with strongly focused laser beams makes this particular setup nearly ideal for the nanoscopic injection and detection of SWs. Emission of both localized and propagating SWs on thin Permalloy (NiFe) films was observed. Due to the greater duty cycle of the pumping system, a sustained coherent emission of selected SW modes was achieved. The BLS counts versus laser power shows a non-linear, stronger than square, dependence. This is in accordance with the square dependence of the counts with the coherent magnon number and the Bloch $T^{3/2}$ law. Strong directional propagation of SWs was demonstrated with propagation up to 4 μm from the center of the excitation spot. The direction can be controlled by tuning the angle of the in-plane component of the applied field. Detailed analysis of the X-shaped caustic mode propagation observed in NiFe is presented at the end of the chapter. The observed caustic angle varied from $66 - 74^{\circ}$ for the 8 GHz mode, with increasing magnetic field strength.

Chapter 3 then focuses on the synchronization characteristics of two-dimensional SHNO arrays. A record-breakingly high quality factor of 170,000 was achieved by synchronizing up to 64 oscillators. Scanning BLS measurement for the 2D array showed that the oscillators in line with the direction of the applied current synchronize first, and are followed by the four chains synchronizing together at higher currents. This is further exploited in the

applicability of the 2D SHNO array to neuromorphic computing. By injection locking the four chains with two radio frequency (RF) inputs at double the oscillator frequency, the synchronization maps shown in Ref. [64] were reproduced. In the last section of the chapter, a unique SHNO-based Ising machine is demonstrated. A 1×2 and a 2×2 array of SHNOs are injection locked using an external RF source at nearly double the oscillator frequency. By modulating the power of the RF input, it is shown that the output power hops between low and high states. Phase-resolved BLS measurements on the two devices clearly show the different phase configurations for a given operating point set by tuning the applied field.

The final chapter summarizes the entire thesis, and the future prospects for the study of non-linear magnetization dynamics using light are discussed.

1

Background and techniques

1.1 Basic Phenomena

1.1.1 Magnetization dynamics

Classically, the magnetic moment $\boldsymbol{m}$ of an atom is defined by the angular momentum $\boldsymbol{L}$ (Eq. 1.1) of the unpaired valance electron orbiting around the nucleus.

$$\boldsymbol{m} = -\gamma \boldsymbol{L}, \tag{1.1}$$

where γ is the gyromagnetic ratio. In the presence of a homogeneous external magnetic field $\boldsymbol{H}$, the magnetic moment experiences a torque $\boldsymbol{\tau} = \frac{\partial \boldsymbol{L}}{\partial t} = \boldsymbol{m} \times \boldsymbol{H}$ perpendicular to both $\boldsymbol{H}$ and $\boldsymbol{m}$. This torque leads to Larmor precession of the magnetic moment around the applied field at a frequency $\omega = -\gamma H$. The precessional torque $\boldsymbol{T_P}$ on the moment is given by the equation

$$\frac{\partial \boldsymbol{m}}{\partial t} = -\gamma \big(\boldsymbol{m} \times \boldsymbol{H}\big) = \boldsymbol{T_P} \tag{1.2}$$

Uniform precession is idealistic, and experience shows the presence of a damping torque that pushes the magnetic moment to align with the applied magnetic field. This damping torque is perpendicular to the precessional torque $(\boldsymbol{m} \times \boldsymbol{H})$ and the magnetic moment $(\boldsymbol{m})$. By introducing a proportionality constant α, in the form of a material-dependent damping parameter, we can write the damping term as:

$$\boldsymbol{T_D} = \frac{-\gamma \alpha}{m} \Big[\boldsymbol{m} \times \big(\boldsymbol{m} \times \boldsymbol{H}\big)\Big] \tag{1.3}$$

By combining the torques in a magnetic system, we can write the equation of motion of the magnetic moment in the presence of a magnetic field known as the Landau–Lifshitz–Gilbert (LLG) equation [65, 66]. It is straightforward to replace the magnetic moment $\boldsymbol{m}$ by the magnetization $\boldsymbol{M}$ for a bulk material. Since several internal fields contribute to the field acting on the magnetic system, we can rewrite $\boldsymbol{H}$ as $\boldsymbol{H}_{\mathit{eff}}$, which is the sum of the demagnetizing field, the Zeeman field, the anisotropy field, the exchange field, and so on. The LLG equation can thus be written as:

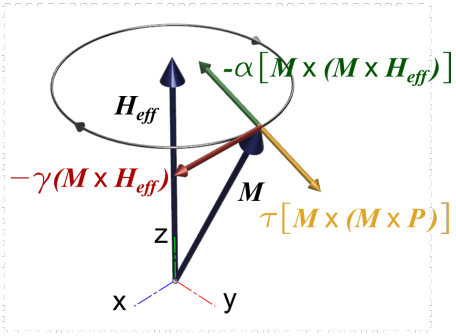

Figure 1.1: Precessional dynamics of the magnetization around the external magnetic field showing the various terms of the LLGS equation.

$$\frac{\partial \boldsymbol{M}}{\partial t} = -\gamma\big(\boldsymbol{M} \times \boldsymbol{H}_{eff}\big) - \frac{\gamma\alpha}{M}\Big[\boldsymbol{M} \times \big(\boldsymbol{M} \times \boldsymbol{H}_{eff}\big)\Big] \tag{1.4}$$

To achieve steady state precession, it is necessary to apply a torque acting opposite to the damping torque in Eq. 1.4. In 1996, Slonczewski [51] and Berger [50] formulated a negative damping term to explain the negative torque that arises in in a magnetic material as a result of the flow of a spin-polarized current, known as spin-transfer torque (STT). The equation of motion then becomes

$$\frac{\partial \boldsymbol{M}}{\partial t} = -\gamma\big(\boldsymbol{M} \times \boldsymbol{H}_{eff}\big) - \frac{\gamma\alpha}{M}\Big[\boldsymbol{M} \times \big(\boldsymbol{M} \times \boldsymbol{H}_{eff}\big)\Big] + \tau\Big[\boldsymbol{M} \times \big(\boldsymbol{M} \times \boldsymbol{P}\big)\Big], \tag{1.5}$$

where $\boldsymbol{P}$ is the spin polarization of the current and τ is the driving torque. Eq. 1.5 is also known as the Landau–Lifshitz–Gilbert–Slonczewski (LLGS) equation, and is the basis for understanding auto-oscillations in spin-torque oscillators (STOs). STOs will be further described in later sections.

Ferromagnetic resonance

The absorption of energy from a transverse RF field is maximum when the frequency of the RF field matches the precessional frequency (Eq. 1.2) of the magnetic moment around the uniform magnetic field vector ($\boldsymbol{H}$) in a ferromagnet. This resonance condition is called ferromagnetic resonance (FMR). The FMR frequency f_0, for a thin film, magnetized in an arbitrary out-of-plane (OOP) angle θ, is given by:

$$f_0 = \frac{\mu_0\gamma}{2\pi}\sqrt{H_{int}(H_{int} + M_0\cos^2\theta_{int})} \tag{1.6}$$

where θ_{int} and H_{int} are the OOP angle and the internal field and arise from the effects of the demagnetizing fields and magnetization anisotropy, which

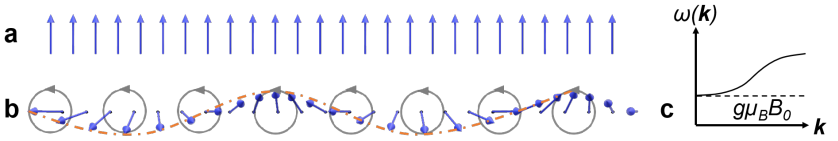

Figure 1.2: Semiclassical representation of spin waves in a one-dimensional spin chain. a) Ground state b) excited state showing spin wave as a collective excitation of precessing spins. c) Spin-wave dispersion relation

can be calculated using specific sets of boundary conditions

$$\begin{aligned} H\cos\theta &= H_{int}\cos\theta_{int} \\ H\sin\theta &= (H_{int}+4\pi M_0)\sin\theta_{int} \end{aligned} \tag{1.7}$$

1.1.2 Spin waves

Spin waves are low-lying collective excitation states in an ordered spin structure, positioned just above the magnetic ground state. Spin waves were first introduced by Bloch in his seminal paper in 1930 [67]. Semiclassically, a 1D spin wave can be represented as a constantly precessing chain of spins around an effective magnetic field with a well-defined phase relation. A schematic representation of spin waves in a one dimensional spin chain is given in Figure 1.2. The wavelength of the spin wave is then given by the length of the chain, where the phase is rotated by 360°.

Spins are better defined by quantum mechanical operators. Based on second quantization principles, one can arrive at quanta of spin waves, called magnons [68]. Let us begin with the Heisenberg Hamiltonian for a simple ferromagnet, given by the equation

$$\mathcal{H} = -\frac{1}{2}\sum_{i,j} J_{ij}\boldsymbol{S}_i\cdot\boldsymbol{S}_j - g\mu_B B_0\sum_i S_i^z, \tag{1.8}$$

where J_{ij} is the exchange interaction between sites i and j, $\boldsymbol{S}_j$ is the spin angular momentum operator of site j, g is the Landé g-factor, μ_B is the Bohr mangneton, and B_0 is the field applied in the z direction. S_i^z is the z-component of the spin angular momentum of site i. By applying the Holstein–Primakoff transformation, which uses the magnon creation ($a_j^\dagger$) and annihilation (a_j) operators and their Fourier transforms $a_{\boldsymbol{k}}^\dagger$ and $a_{\boldsymbol{k}}$, we can rewrite Eq. 1.8 in the reciprocal space as

$$\mathcal{H} = A_0 + \sum_{\boldsymbol{k}} \omega(\boldsymbol{k}) a_{\boldsymbol{k}}^\dagger a_{\boldsymbol{k}} \qquad \text{and} \tag{1.9}$$

$$\omega(\boldsymbol{k}) = g\mu_B B_0 + \langle S^z\rangle[J(0) - J(\boldsymbol{k})] \tag{1.10}$$

A_0 is a constant that is independent of the creation and annihilation operators and represents the ground state energy. The second term in Eq. 1.9 represents quasiparticle excitations of frequency $\omega(\boldsymbol{k})$. In the low temperature limit,

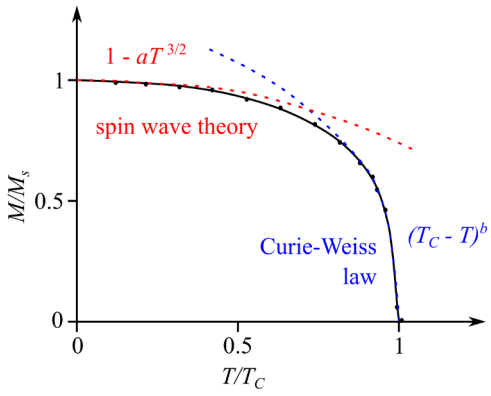

Figure 1.3: Spontaneous magnetization of a ferromagnet against temperature.

$\langle S^z \rangle \longrightarrow S$. Eq. 1.10 is the spin wave dispersion relation. In the low temperature approximation, the spin-wave dispersion is depicted in Figure 1.2.c, where $g\mu_B B_0$ represents the magnon band gap.

Bloch $T^{3/2}$ law

The magnetization (M) of a ferromagnet decreases as a function of increasing temperature, as shown in Figure 1.3 (Note: M is normalized with the spontaneous magnetization (M_s), which is the magnetization at absolute zero). According to Weiss theory, the origin of order in ferromagnets lies in an effective molecular field that arises from the alignment of the magnetic moments. At a particular critical temperature, the Curie temperature (T_C), the spontaneous magnetization approaches zero. In Figure 1.3, the magnetization is proportional to $(T_C - T)^b$ (represented by the blue dotted line) near the critical region ($T = T_C$), where b is the critical exponent. The deviation from the Curie–Weiss law observed at low temperatures can be explained using the spin wave theory developed by Bloch. The number of magnons (n_m) at a given temperature T is given by

$$n_m = \int_0^\infty \frac{g(\omega)d\omega}{exp(\hbar\omega/k_B T) - 1} \tag{1.11}$$

Here the density of states, $g(\omega)$, is proportional to the square root of the angular frequency ω at low temperatures. By replacing $g(\omega)$ by $\omega^{1/2}$ and solving the resulting integral, we arrive at the relation

$$\frac{M_s - M}{M_s} = aT^{3/2}, \tag{1.12}$$

where a is the proportionality constant. Figure 1.3 shows the red dotted line which fits the curve of M against T quite accurately at low temperatures.

1.1.3 Spin Hall Nano-Oscillators

Spin-polarized charge currents, or pure spin currents, flowing through a magnetic layer can induce a torque on the local magnetization, called the spin-transfer torque (STT). In Section 1.1.1, we have seen that the precessional dynamics of a magnetic layer can be sustained by introducing a torque (such as the STT) in the direction opposite to the damping torque. Sustained magnetization precession, also known as auto-oscillations (AO), are intense nonlinear spin wave processes and require high (spin) current densities. Advances in nanofabrication methods have made it possible to achieve such high current densities in nanoscale devices. Devices that work on the STT principle to achieve auto-oscillation are known as spin torque oscillators (STOs), and can be broadly classified as spin torque nano-oscillators (STNOs) and spin Hall nano-oscillators (SHNOs) [61, 62, 69–72]. The operation of STNOs is based on spin polarized currents generated by the STT, while SHNOs make use of the spin Hall effect [73–76] (SHE) to generate pure spin currents. Several sample geometries have been fabricated and studied by various groups.

This thesis focuses on one particular device geometry—a nanoconstriction of a HM–FM bilayer. Nanoconstriction-based SHNOs were first designed by Demidov et al. [62]; in these devices, current flowing through the HM layer results in spin accumulation on its two interfaces, as a result of the strong spin–orbit (SO) coupling. The diffusion of spins from the HM layer to the FM layer occurs at the HM–FM interface, causing a transverse flow of spin current in the device, thus exciting the dynamics in the magnetic system (Eq. 1.5). The spin diffusion process, however, is not lossless [77–80]: its efficiency is given by the ratio of the diffused spin current to the injected charge current, denoted by ξ_{SH}. This ratio is always smaller than the conventional spin Hall angle (θ_{SH}), which is the ratio of the spin and charge current densities in the given HM layer.

In Ref. [62] a NiFe/Pt bilayer was etched into a small nanoconstriction. The spin current flowing from the Pt layer into the NiFe layer induces auto-oscillation of the magnetization vector. The oscillating magnetization modifies the resistance at the same frequency through anisotropic magnetoresistance (AMR). The product of the oscillating resistance and the charge current then appears as a microwave voltage across the two contact electrodes. The signal can then be examined with a spectrum analyser. The origin of the AO modes, based on the potential well created by the nonuniformity of the internal static magnetic field, is explained by Dvornik et al. [81]. Since the read-out from an SHNO depends on the AMR of the sample, which is much smaller than GMR or TMR, the power of the microwave output is much smaller. However, the ease of the design allows one to improve the output by fabricating many devices laterally and operating them in a synchronized regime. SHNOs also provide a direct way to study the AO modes with optical techniques, such as Brillouin light scattering (BLS) and the magneto-optical Kerr effect (MOKE).

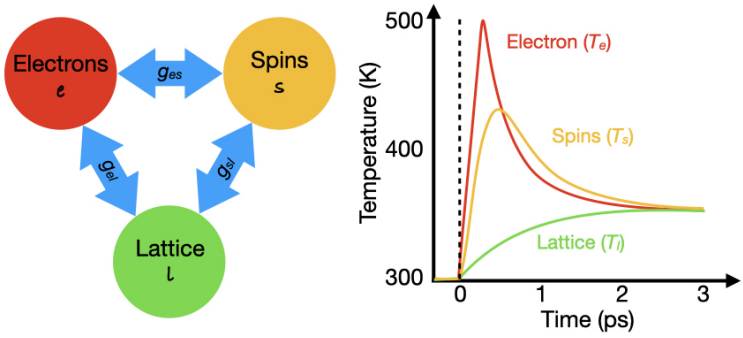

Figure 1.4: Schematic representation of the phenomenological three-temperature model and a plot showing the effective timescales of excitation and relaxation for the three temperature baths.

1.1.4 Rapid demagnetization

More than two decades ago, the first experimental observation of ultrafast demagnetization, on a subpicosecond time scale, was reported by Beaurepaire et al. [1], leading to a new branch of magnetism where the magnetization dynamics are excited and observed on unprecedentedly short timescales. The pioneering experiment was performed on a Ni thin film, where the sample was irradiated by 60 fs Ti:Sa laser pulses and the dynamics was observed using the stroboscopic technique of the time-resolved Magneto-optical Kerr effect (TR-MOKE). A phenomenological three-temperature model (3TM) was used to describe the observed dynamical properties, where the temperatures of electrons (T_e), spins (T_s), and lattice (T_l) interact with each other on different timescales (due to the different coupling constants g_{es}, g_{sl}, and g_{el} between the three subsystems), leading to the observed rapid demagnetization phenomenon (see Figure 1.4). A microscopic implementation of the 3TM was formulated by Koopmans et al. [82], as is referred to as the M3TM. In this model, the spin relaxation is mediated by Elliott–Yafet (EY) spin-flip processes for electron–phonon scattering events, where the probability of the spin-flip process is denoted by a_{sf}. By applying Fermi's golden rule for the Hamiltonian of the system and solving the rate equations, we arrive at the set of differential equations given below, which can be used to fit the experimental data and obtain the spin-flip scattering probability for a given material.

$$C_e \frac{dT_e}{dt} = -g_{el}(T_e - T_l) + P(t), \tag{1.13}$$

$$C_l \frac{dT_l}{dt} = g_{el}(T_e - T_l) \tag{1.14}$$

$$\frac{dm}{dt} = Rm\frac{T_l}{T_C}\left[1 - m\coth\left(\frac{mT_C}{T_e}\right)\right] \tag{1.15}$$

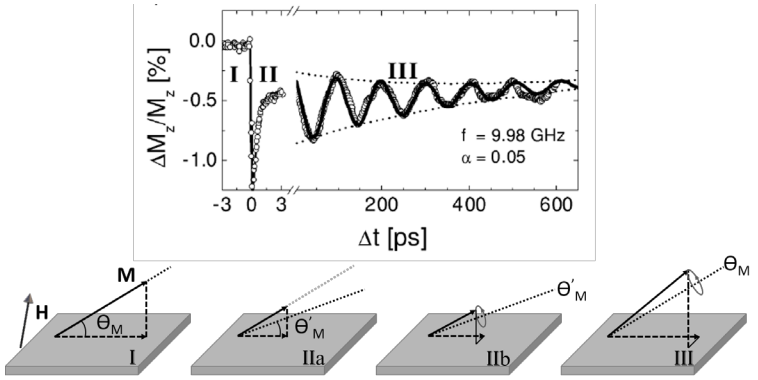

Figure 1.5: Effects of ultrashort laser pulses on metallic ferromagnets. Figure adapted from [3] with permission.

C_e and C_l are the specific heat capacities of the electron and the phonon subsystems. T_C is the Curie temperature of the ferromagnetic material. $m = M/M_s$ is the relative magnetization. R is a material-specific scaling factor given by the relation

$$R \propto a_{sf} \frac{T_C^2}{\mu_{at}}, \tag{1.16}$$

where μ_{at} is the atomic magnetic moment.

Several important physical phenomena have been observed as a consequence of femtosecond laser excitation of magnetic materials. While the quenching of the magnetic moment, in typically less than a picosecond, is the primary effect in ferromagnetic metals, it is also possible to launch spin waves on the nanosecond timescale [3]. Additionally, in antiferromagnetic materials, a phase transition can be detected, where the ordering of the magnetic moments undergoes a transition from antiferromagnetic to ferromagnetic upon laser excitation. The switching of magnetic moments due to circularly polarized light and their toggle switching due to linear polarized light, as seen in ferrimagnets, have given rise to new technological possibilities, where ultrashort laser pulses can be utilized to achieve the fastest ever switching of magnetic domains in magnetic recording media.

For thin ferromagnetic films with the external field pointing out-of-plane (OOP), the magnetization $\boldsymbol{M}$ at equilibrium is directed at an angle θ_M OOP, as depicted in Figure 1.5.I. Upon laser excitation by a femtosecond laser pulse, the energy from the photons is absorbed by the electrons, which are rapidly thermalized. The almost instantaneous temperature increase of the electrons causes the magnetic moments to quench, and the material is demagnetized in about 50–100 femtoseconds. A new equilibrium angle, θ'_M, depicted in Figure 1.5.IIa, is then defined by the new effective field, resulting from both a loss of demagnetization field and a possible change in anisotropy strength. In region IIb, the magnetization precesses around the equilibrium orientation, while $|\boldsymbol{M}|$ relaxes back, typically on the timescale of a few tens of picoseconds.

Over a longer timescale, from subnanoseconds to a few nanoseconds (Region III), the magnetization precesses coherently around the equilibrium angle and, due to inherent damping in the material, the magnetization eventually realigns with the original effective magnetic field. The data in Figure 1.5 is reproduced from Ref. [3].

1.1.5 Light scattering by magnons

The scattering of light is a phenomenon where an electromagnetic wave with a certain energy E_{in} and wave vector k_{in} is incident on a particle, and is absorbed and then re-emitted with either the same or different energy E_{out} and momentum k_{out}. The difference between the energies, on the one hand, and the momenta on the other, of the incident and scattered beams, are the energy and momentum absorbed or emitted by the particle, based on their respective conservation laws. Scattering can be classified into two main categories: elastic scattering, such as reflection and Rayleigh-like scattering, where $\Delta E = E_{out} - E_{in} = 0$, and inelastic scattering, such as Raman and Brillouin scattering, where $\Delta E \neq 0$. Inelastic scattering can be further separated into Stokes and anti-Stokes scattering, in which the energy of the scattered light is respectively less or greater.

The inelastic scattering of light by magnons and acoustic phonons is called Brillouin light scattering (BLS). In contrast to Raman scattering, which is mostly due to optical phonons in solids or vibrational modes of molecules in liquids, in the range of THz, magnons and acoustic phonons fall into the MHz, GHz, and sub-THz region. Since the wavevector of visible light is much smaller than that of magnons or phonons, only those phonons or magnons close to the Brillouin zone center can be detected. The general mechanism of scattering of light in solids depends on the variation in the permittivity tensor. In inelastic scattering, the variation of the permittivity, leading to induced dipoles, radiates light with a different energy. The change in energy is related to the energy of the created or annihilated mode. In the case of phonons, the polarization of the light is preserved. However, the selection rules in magnetic states result in the rotation of the light's polarization by 90 degrees. We can thus study phonons and magnons separately.

The intensity of the scattered light is given by the square of the electric field (E). Since BLS is a time averaged technique, the measured BLS intensity (I_{BLS}) is proportional to $\langle (E)^2 \rangle$. Consider a set of N scatterers where E_i is the electric field component of the i^{th} scatterer. For this case $I_{\mathrm{BLS}} \propto \langle (\sum E_i)^2 \rangle$. If the N scatterers are incoherent, then $I_{B\mathrm{BLS}} \propto \langle \sum E_i^2 \rangle$ since $\langle E_i E_j \rangle = 0$ for $i \neq j$. Contrarily, if the N scatterers are coherent, then $\langle E_i E_j \rangle = \langle E_i^2 \rangle$. In our case N is the number of magnons. Hence the BLS intensity for incoherent magnons is proportional to N and in-phase coherent magnons show $I_{\mathrm{BLS}} \propto N^2$ and a destructive interference gives zero BLS intensity.

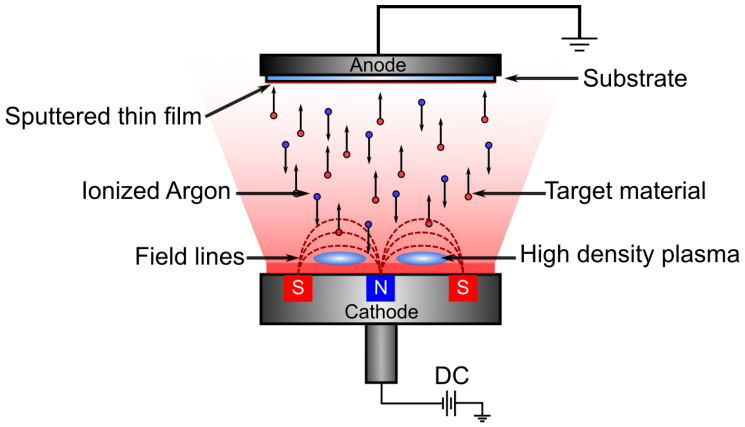

Figure 1.6: A schematic representation of the process of magnetron sputtering.

1.2 Experimental Techniques

1.2.1 Deposition of thin films

The study samples were deposited on to a sapphire or silicon substrate using a technique called sputtering, which involves the deposition of atoms or molecules onto a substrate after being ejected from a target through bombardment with high energy particles (plasma). The entire process takes place in a high vacuum controlled chamber filled with inert gas (typically argon) at around 3 mTorr pressure. In this present thesis, an AJA Phase II magnetron sputtering device was employed. Magnetron sputtering techniques use a magnet behind the cathode to trap the free electrons from bombarding the substrate (See Figure 1.6). This technique has the advantage of higher sputtering rates than conventional sputtering systems. An AJA phase II system consists of seven confocal sputtering guns arranged in a circular fashion at the bottom of the vacuum chamber. It uses both DC and RF sources to excite plasma around metal and insulator targets, with three guns being available for use at one time. The substrate is loaded upside down using a manipulator via a load–lock. This technique also produces higher-quality thin film than evaporation methods. A 20 mm $\times$ 20 mm epipolished c-plane sapphire substrate was chosen. This choice of substrate was deliberate, in order to avoid thermalization issues resulting from the absorption of energy from the focused laser spots. Since sapphire transmits nearly 90% of the light in the visible through ultraviolet range, almost no electromagnetic energy is absorbed from the two lasers. Sapphire is also a better conductor of heat than conventional silicon oxide wafers. Different layers of thin films were sputtered in situ without breaking the vacuum. The NiFe layers were coated with SiOx capping to avoid oxidation of the metallic surface.

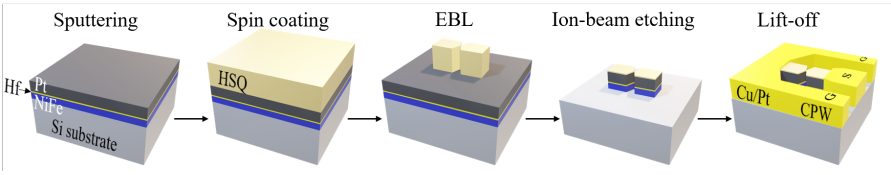

Figure 1.7: Fabrication line of spin Hall nano-oscillator arrays

1.2.2 Fabrication of SHNO

A detailed description of the fabrication steps for different types of SHNO devices can be found in [83–85]. Figure 1.7 shows the step-by-step process. The sputtering chamber was maintained under high vacuum with a constant flow of Ar at 3 mTorr pressure. $Ni_{80}Fe_{20}$ (3 nm), Hf (0.5 nm), and Pt (5 nm) were sputtered on a highly resistive silicon substrate with six times greater thermal conductivity than sapphire. The Hf interlayer improved the magnetodynamic properties of the soft ferromagnetic layer [86]. The layers were then covered by hydrogen silsesquioxane (HSQ) resist by spin coating, and the constriction pattern was written onto this using an electron-beam lithography machine at 100 kV (Raith EBPG 5200). The exposure rate was set to 2000 $\mu C/cm^2$. The sample was dipped into a developer solution to remove the unexposed parts. Using an ion beam etching process at 30° incident angle to the film normal, the patterns were transferred onto the trilayer. A thin layer of silicon dioxide remained on the constriction region as protection againt oxidation. To make effective CPW contacts, a positive photoresist was deposited and defined by optical lithography. A very short exposure to buffer HF (BOE) suffices to remove the oxide layer at the end of the mesa, in order to fabricate the electrical contacts. The sample was loaded into the sputtering chamber, where 700 nm Cu and 20 nm Pt were sputtered consecutively. The excess was then removed by lift-off process using a warm resist remover. As a final step, the sample was sequentially immersed in isopropanol and distilled water to ensure removal of the residual particles.

1.2.3 Microwave measurement setup

The read out of the auto-oscillations in SHNOs is based on the oscillating resistance of the sample base on the AMR. A custom-made probe was used to pass a DC current through the constriction and read out the microwave voltage. The device was placed in the presence of an external magnetic field (GMW Associates) applied at an oblique azimuthal or OOP angle from the surface of the device, θ; ϕ is the IP angle measured from the line passing perpendicular to the flow of current. As the spin current transfers from the heavy metal layer to the ferromagnetic layer, negative damping causes self-sustained oscillations of the magnetic moment. The AMR effect causes the precession to give rise to an oscillating resistance at the same frequency. The oscillating resistance thus results in an oscillating voltage in the GHz range. Using a bias-tee, the DC

and RF components of the voltage are separated and sent respectively to a sourcemeter and a spectrum analyzer. Since the signal due to AMR is weak, the RF signal is amplified with a low noise amplifier (LNA) before being captured by a Rhode & Schwarz FSV-40 spectrum analyzer. Previously chosen values of resolution bandwidth (RBW) and video bandwidth (VBW) were used to capture meaningful values of linewidth and power. To remove the background noise, a spectrum was captured at a very low current prior to analysis, and subsequently subtracted from the actual spectra to obtain clean AO spectra. The data presented are in dB over noise (or simply dB). The measured PSDs are fitted to symmetric Lorentzian functions to determine the peak frequency, signal coherency (linewidth), and peak power. A Keithley 2450 sourcemeter was used as a current source and a voltmeter for the DC measurements.

Injection locking

Two signal generators (Rhode & Schwarz SMA 100B units) were coupled to the above setup, with a signal coupler and a circulator to inject external signals, in order to lock the SHNOs to specific frequencies definded by the external signal; injection locking was always done at twice the frequency of the SHNO. This is called parametric pumping of the oscillators. The circulator is used to prevent the external signal from burning the LNA. Extra precautions were also taken by choosing the operational bandwidth of the LNA to be much lower than the pumping frequency of the external RF signal.

1.2.4 Brillouin light scattering microscopy ($\mu-$BLS)

A significant part of the study of magnetization dynamics in this thesis was conducted using a $\mu-$BLS setup. BLS microscopy can measure the amplitude and the spectrum of the spinwaves in a microscopic area. A linearly polarized continuous wave laser (532 nm) is focused down to the diffraction limit on the sample under a microscope objective. The light that is scattered back from the sample is collected through the same objective. While most of the light undergoes a Rayleigh type scattering, a small portion is scattered from the magnons and acoustic phonons. The photons either gain energy (anti-Stokes) or lose energy (Stokes) from the inelastic scattering. Since the polarization of the light scattered from magnons is rotated by 90°, we can filter this out using a high extinction-ratio polarizer. The back scattered light is then directed onto a six-pass Tandem Fabry-Pérot Interferometer (TFPI), which analyses the shift in frequency by comparing it with a reference signal that is fed directly into the device. BLS microscopy consists of four parts:

1. Probe laser setup
2. Illumination optics
3. Stabilization system
4. Interferometry

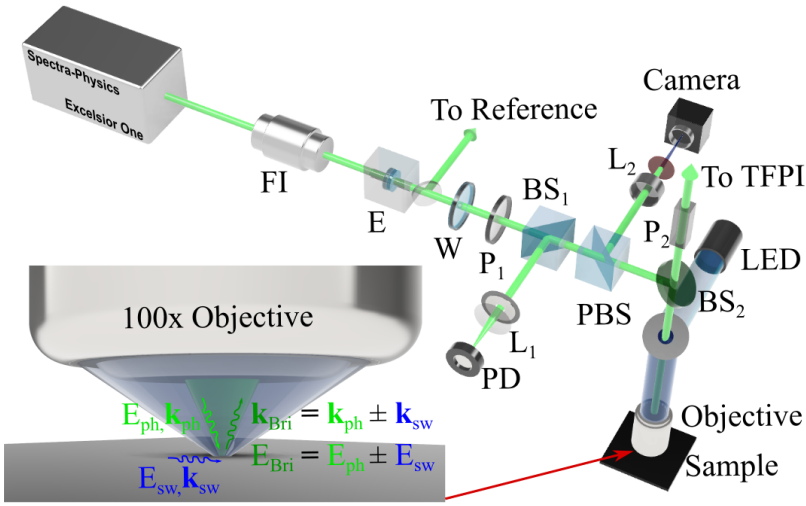

Figure 1.8: Probe system using a continuous wave 532 nm green laser. The optical components used in the setup are FI: Faraday isolator; E: etalon; W: $\lambda/2$ waveplate; P: polarizer; BS: beam splitter; PBS: polarizing beam splitter; L: lens; and PD: photo detector. The close up view of the sample shows the scattering process occurring at the sample, and the equation represents the law of conservation of energy and momentum.

Probe laser setup

The probe laser is a frequency-stabilized solid-state laser operating at 532 nm wavelength with an extremely narrow bandwidth of less than 10 MHz (the Spectra Physics Excelsior 300 mW laser). The output polarization from the laser is s-polarized. To avoid thermal instabilities due to reflection back into the laser, an optical diode (Thorlabs IO-3-532-LP) was used immediately after the laser cavity (see Figure 1.8). A thermally stabilized etalon filter (TCF-2 from Table Stable) suppresses spurious sideband modes that might be present in the otherwise highly monochromatic laser. A portion of the laser is then deflected onto the TFPI as the reference beam using a beamsplitter (BS). The intensity of the laser is controlled by a combination of $\lambda/2-$waveplate and a film polarizer. The light is then directed through a Polarizing beamsplitter cube into a 100× microscope objective (Zeiss-EC Epiplan Neofluar) with a numerical aperture of 0.75. The scattered light is collected back through the same objective. This implies that the maximum cone angle of the focusing light is 49°; subsequently, the maximum k-vector that can be detected by the instrument is limited to $k_{sw}^{max} = 17.8$ rad/μm. Correspondingly, the shortest detectable wavelength of the spin wave is $\lambda_{sw}^{min} = 350$ nm. The back-scattered light passes through a Glan–Thompson polarizer with an extinction ratio of better than 100000:1. The orientation of the polarizer can be adjusted to let through the light scattered either from magnons or from phonons.

Illumination optics

To study devices such as SHNOs, the need to image the nanodevice is of paramount importance for two reasons: First, to ensure that the laser is focused on the right device. Second, to use the image as a feedback to stabilize the stage, which has a fairly large thermal drift over a long period of time. A 470 nm (blue) LED was used as the illumination source. The blue light was collimated and reflected off a holed mirror into the same objective in a dark-field geometry. The light entering through the sides of the objective was collected back from the center and passed through the hole in the holed mirror. The reflected light was then focused onto the CCD plane with the help of an infinity-corrected lens. A bandpass filter for 470 nm was used to allow only blue LED light though, hence avoiding saturation by the more intense green laser. However, since visualization of the green laser spot is necessary to position the sample, the filter F was tilted slightly to allow 0.1% of the laser light through. The CCD used in the setup was a Point Grey Flea3 USB3 (FL3-U3-13Y3M-C) with a quantum efficiency of 61% at 525 nm. The lenses were chosen such that the surface area of the sensor was filled approximately with 2000 μm^2 of the sample plane.

Stabilization system

Stabilization of the system plays an important role in an experiment where sensitivity is very high. A small disturbance can amplify noise in the measured spectra exponentially. As a first step, the entire optical layout was arranged on air suspension stabilizers with active stabilization. The positioning of the sample was performed using a triple axis Newport XPS Q8 motion controller. A closed feedback loop with PID controllers was used to actively stabilize the stage with a maximum noise level of no more than 10 nm. Since the diffraction limit of the 532 nm green laser is $\approx$260 nm, a 10 nm noise in the sample position represents less than a 5% error in the position of the sample. A much larger error arises from external factors, such as vibrations and thermal instabilities. To reduce the drift due to these external factors, a continuous feedback system is used, whereby the stage corrects its position based on the reference image of part of the sample. However, this only works in the x and y directions—that is, in the plane of the sample. To correct for the instabilities in the focus plane, a small portion of the Rayleigh peak is deflected from a beamsplitter and focused onto a photodiode through a pinhole. By scanning the z-stage at regular intervals, we are able to find the point of maximum amplitude, which corresponds to the position of the z-stage at the focal plane. The sample stage was placed directly above a customized magnet (GMW Associates), which produced an oblique magnetic field. The calibration of the magnet was performed at the focal point of the laser spot using a 3D-Hall probe (Senis).

TFPI

The interferometer is a commercially available six-pass TFPI with two Fabry-Pérot pairs (TFP-1 from Table Stable). The beam back-scattered from the sample after polarization filtering constitutes shifts in the energy of the photon in the GHz range, as the magnon energies are typically in the GHz range. Detection of such small frequency shifts with a high precision is so far only possible with a high-end Sandercock-type interferometer, as mentioned above, which has a measuring range from a few hundreds of MHz up to a THz, depending on the distance between the FP mirrors. The high quality mirrors used in the instruments suppresses the sidebands up to 10^{-15}. The sample beam is spatially filtered by focusing it through a pin hole (the input slit) and then collimating it with a lens. The beam subsequently passes through each of the mirror pairs three times. The etalons are actively stabilized by piezoelectric actuators. FPIs work on the principle that, for a given mirror spacing d, only those wavelengths λ that satisfy the condition

$$d = \frac{1}{2}p\lambda \qquad \forall p = 1, 2, 3, ... \tag{1.17}$$

pass through, with other wavelengths being diminished. Spectrally filtered light is detected by an avalanche photodiode (APD) (Count-10B, Laser Components AB), which is a high sensitivity detector with a quantum efficiency of nearly 80%. The distance between the mirrors are scanned by piezos, and each spacing corresponds to a particular wavelength channel. The shift in frequency is then calculated by letting the reference light through, and calculating the mirror distance corresponding to the transmission of the reference light. The entire scanning stage holding the two mirrors is placed on piezoelectric stabilizers to reduce external noise. Finally, the coordinated operation of this complex system is controlled by a software solution from THATec Innovation.

1.2.5 High repetition-rate femtosecond laser setup

To excite dynamics in the magnetization of thin film, we have integrated the existing $\mu-$BLS setup with a high repetition rate femtosecond pulsed laser capable of scanning spatially on the surface of the sample (as shown in Figure 1.9). The pulsed laser is directed through a set of lenses and a pair of galvomirrors to enable lateral movement of the laser spot on the sample. The pulsed laser is focused using the same objective as the green laser. A small portion of the laser that is reflected back through the objective is directed to the camera to visualize the laser spot.

Pump laser setup

A commercially available Ti:Sa Taccor Power laser with 1 GHz repetition rate was procured (Laser Quantum). The laser pulse duration was measured to be 30 fs, and the maximum average power of the laser was 2 W. A broadband Faraday isolator was used to block reflections back into the laser cavity. An achromatic $\frac{\lambda}{2}-$waveplate was mounted on a motorized rotational holder to

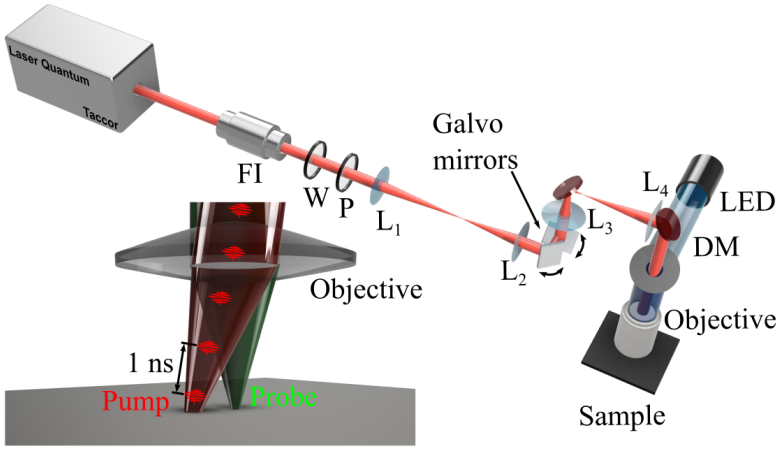

Figure 1.9: Pump system using a GHz repetition rate femtosecond pulsed laser. FI: Faraday isolator; W: $\lambda/2$ waveplate; P: polarizer; L_{1-4}: scanning lens systeml and DM: dichroic mirror. Using the galvomirrors and the lens system, the angle of incidence of the light onto the aperture of the objective can be controlled, and can hence control the relative position of the pump spot with respect to the probe spot.

be used in combination with the Faraday isolator to control the power of the laser.

Scanning laser optics

The scanning system is a set of four lenses and a pair of mirror galvanometers. The four lenses were arranged so that the image plane of the first two lenses was exactly at the center of the pair of Galvo mirrors, and also formed a conjugate plane with the plane of the objective entrance slit and the last two lenses. In this way, the angle of the input beam at the entrance slit was slightly tilted without altering the beam divergence or the diameter. The small change in the tilt reciprocates as a change in the lateral position of the pump laser spot. Calculations show that the maximum change in the angle of the focused beam is less than 1° from the normal incidence. Hence, the change in the k-vector of the incident beam for a lateral displacement of 10 μm on the sample is negligible. Additionally, the beam diameter can also be changed using the two lenses before the mirror galvanometers. The lateral motion of the laser spot was well calibrated using a calibration target, consisting of a grid pattern of 5×5 µm^2 islands of Au with a height of 50 nm on a sapphire substrate. This pattern was etched using EBL in order to achieve high precision cuts for the edges of the islands.

1.2.6 Automation of data acquisition

Finally, to control and perform automated measurements, we used a server-based software solution (THATec Innovation). All the instruments are controlled individually by separate programs in LabVIEW, and each instrument can be connected to the main THATec:OS GUI operating system, which is based on a server. The process can be structured simply by dragging and dropping, allowing measurements to easily be automated on very fast timescales. The software also allows data to be visualized and some basic analysis to be performed. However, more detailed analysis was carried out later using Matlab and OriginLab software.

2

Spin wave emission using frequency combs

In the search for compact, faster, and more energy efficient alternatives to CMOS-based electronic devices, researchers have discovered new branches of physics, such as spintronics, magnonics, and photonics. Magnonics is a very young field with rich physics and an increasing number of novel phenomena. It aims to control and manipulate SWs in ferromagnetic, ferrimagnetic, and antiferromagnetic materials that could be used for computing purposes by designing NOR, XNOR, and other logic gates [28–31]. The magnetic excitations are typically in the range of GHz frequencies in ferromagnetic and ferrimagnetic materials, and in the THz range in antiferromagnetic materials, thus allowing much faster device operation than conventional electronics. Since the wavelength of the SWs can be orders of magnitude smaller than their electromagnetic counterparts in the frequency range, it is possible to minimize the size of these devices [28, 87].

SWs can be excited using a wide range of mechanisms. While the most straightforward and conventional SW generation mechanism is that of an externally applied microwave field using RF antennas [32–34], spin transfer-torque and spin Hall effects generated by direct currents through nanodevices have recently made it possible to generate truly short wavelength, highly nonlinear, very high intensity SWs on the nanoscale [35–43]. A third, contactless alternative is to excite SWs optically using focused femtosecond laser (fs-laser) pulses, inducing rapid demagnetization [1, 88, 89] of the local magnetization [2, 3, 10, 90–93]. Single-pulse excitation schemes, where the system relaxes into equilibrium before the arrival of the second pulse, have been studied extensively in metals [3, 12–14, 44] and dielectrics [11, 45, 46]. The physical mechanism for rapid demagnetization differs quite significantly in metals and insulators. While rapid thermalization of the electrons occur in the former, the inverse Faraday effect (IFE)/photomagnetic effect is dominant in the latter.

SWs are emitted about ≈1–2 ns after the arrival of the pump pulse, and typically have a decay time constant of a few nanoseconds. Traditional pump-probe measurements have been carried out with a repetition rate of 80 MHz or lower, where the time duration between the two pulses is 12 ns or more. SWs

excited using such low repetition rate lasers will be damped out before the arrival of the next pulse. One way to avoid this is to use two identical pump lasers, such that the time between two consecutive pulses can be tailored to achieve coherent excitation. The first attempts to do this [47–49] have shown that, when the phase of the light matches that of the spin wave, the amplitude is doubled by constructive interference. On the other hand, when the phase is off by 90°, destructive interference leads to quenching of the spin wave amplitude. However, the overall duty cycle was not improved.

A much simpler experimental approach is to increase the fs-laser repetition rate to approach the time scale of the SW decay. Frequency-comb fs-lasers with GHz repetition rates have recently become commercially available, and the earliest studies of high repetition rate SW excitations in thick extended iron-garnet films have been reported [15, 16]. Using the inverse Faraday effect for excitation with a 10 μm laser spot, and a conventional time-resolved magneto-optic Kerr effect (TR-MOKE) pump-probe technique for detection, the authors were able to demonstrate coherently amplified excitation of SWs whose phase relation matched the time between consecutive pulses.

Most all-optical studies conducted so far have used stroboscopic pump-probe techniques, such as TR-MOKE or the Faraday effect, to study the immediate SW response after each individual pulse. However, time-averaged techniques, such as Brillouin Light Scattering (BLS) microscopy, have been inadequate due to the low duty cycle. Most TR-MOKE experiments yield a highly resolved temporal picture of the coherent evolution of the magnetic state, but could not detect either incoherent (e.g., thermal) magnons or other excitations, such as phonons. BLS microscopy, on the other hand, is an extremely versatile and sensitive technique, with a very wide frequency range, good spectral resolution, simultaneous detection of coherent and incoherent dynamics, and high wavevector resolution [63, 94–96]. As an added benefit, this also allows for simultaneous detection of both magnetic and nonmagnetic excitations (such as phonons) with the same frequency and spatial resolution [97]. It would thus be highly advantageous to use BLS microscopy to study fs-laser-induced SW excitations, which would require a higher duty cycle, *i.e.* much shorter time in-between laser pulses.

2.1 Frequency-comb-enhanced BLS Microscopy

Manuscript I: BLS microscopy has already been discussed in Sec. 1.2.4. BLS is a highly sensitive technique for measuring acoustic phonons and magnons in many different research areas, a fact which increases the complexity of the instrument. The small frequency shifts (from MHz to GHz), as well as low scattering cross-sections in the case of magnetic transitions, requires an ultra-narrow spectral filter with strong suppression of the side bands. A Sandercock type six-pass TFPI is the standard instrument capable of such a measurement with long integration times. Other faster techniques include highly dispersive virtual-image phase array spectrometers, where speed is achieved at the cost of spectral range and sensitivity.

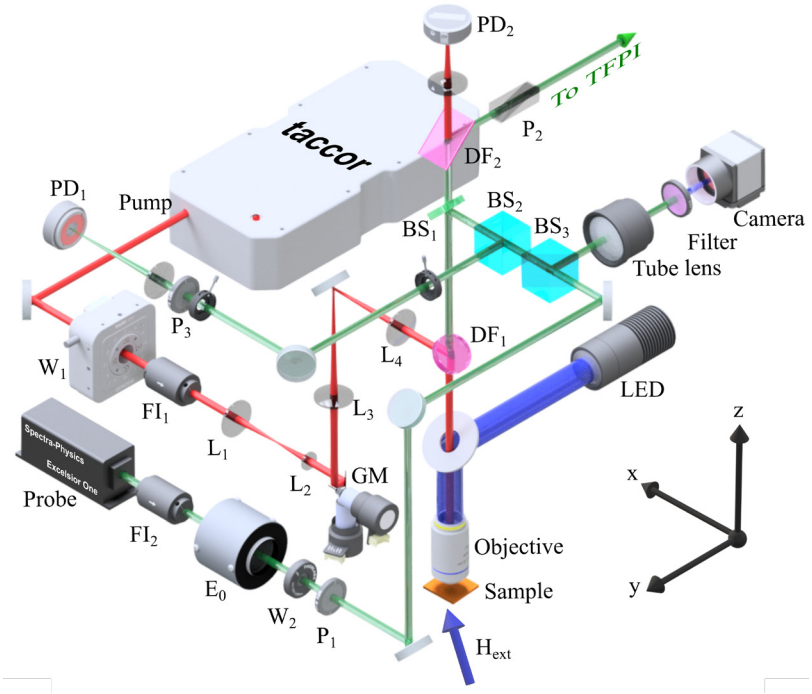

Figure 2.1: Integrated pump–probe system using a CW green laser and a GHz repetition rate femtosecond pulsed laser. W_1 - Motorized waveplate, W_2 - halfwave plate, FI - Faraday Isolator, L - lenses, P - polarizer, DF - Dichroic Filter, BS - beamsplitter, E - Etalon, PD - photodiode and GM - galvanometer. An external magnetic field (H_{ext}) is applied to the sample at an oblique angle.

Mode-locked femtosecond pulsed lasers has been vastly useful in Raman spectroscopy and Brillouin spectroscopy for optical and acoustic phonons respectively, leading to more sensitive and selective measurement techniques such as stimulated Raman/Brillouin spectroscopy. However, to study magnons using TFPI, pulsed lasers have not been very useful due to the low duty cycle of the measurement using a low repetition rate fs-laser. With the advances in frequency comb techniques, pulsed lasers with GHz repetition rates are now available as turn-key operation units. Frequency-comb-enhanced BLS microscopy is a unique technique combining the sensitivity of BLS microscopy as well as the mode selectivity of using a femtosecond pulsed laser. Using this, we are able to coherently excite enhanced vibrational and magnetic modes in the sample that match the harmonics of the repetition rate.

Figure 2.1 depicts a complete optical layout of the frequency-comb-enhanced BLS microscopy. The individual components have been described in Sections 1.2.4 and 1.2.5. It consists of a CW 532 nm laser (green lines) used as a probe. The inelastically back-scattered light is directed to the TFPI for further analysis. The pump laser system (red lines) is intertwined with the

BLS microscope and consists of a scanning system with four lenses and a pair of galvanometer mirrors to control the relative distance between the focused pump and the probe spots on the sample. A blue LED is used along with a holed mirror to obtain a dark-field image of structured samples. The sample is placed on a three-axis nanopositioning stage. A constant magnetic field of up to 1 T (H_{ext}) can be applied obliquely onto the sample using a customized electromagnet. All components are connected and operated through a server using automation solutions from THATec Innovation. More details on this can be found in **Manuscript I:** in the thesis.

2.1.1 Calibration of galvanometer mirrors and the focal position offset

The focal distance and the galvanometer mirrors were calibrated by the knife-edge method [98] using an Au thin film with precisely cut edges. The calibration sample is an array of $5 \times 5\mu m^2$ islands of Pt with a separation of $10\mu m$ from center to center of adjacent islands. The etching was performed by EBL to obtain a high-precision step function. The sample was carefully aligned under the microscope and the beam scanned across the edge. The amplitude of the Rayleigh scattered light thus acquired (by PD_1 for green and PD_2 for red in Figure 2.1) is then the convolution of the step function with the Gaussian beam profile of the laser. The focal plane is obtained by fitting the error function for all the scan measurements along x and y directions for different z, and extracting the minimum beam waist, as shown in the Figure 2.2 (a). The spot diameter at the best focus was found to be 313±11 nm for the green laser and an average of 716±146 nm for the red laser, owing to the ellipticity of 1.07 of the pulsed laser beam.

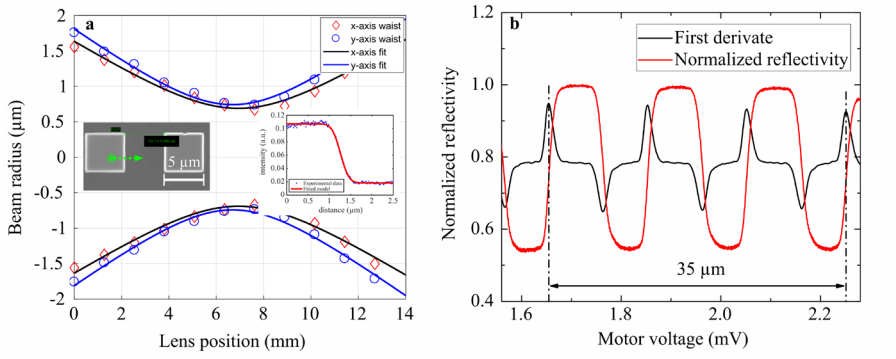

Figure 2.2: **a**. Measurement of beam waist using a knife-edge method with a home-fabricated sample shown in the inset for different values of z. The plot in the inset shows the error function for one such scan. **b**. Calibration of the galvanometer mirrors using the same calibration sample, showing the reflection signal as a function of the voltage applied to the motors.

To calibrate the voltage supplied to the galvanometer mirror, we used the calibration sample described earlier to measure the lateral movement of the pump beam spot corresponding to a given voltage applied to the mirrors. Figure 2.2 (b) shows the amplitude of reflection when the laser was scanned over the matrix of islands. The first derivative of the signal was used to measure the voltage corresponding to a given distance accurately. A maximum thermal drift of 53 nm/°C was estimated, which in practice affects long measurements.

2.2 Sustained *k*–vector Selective Emission of Spin Waves in NiFe Thin Films

Manuscript II: Earlier in this chapter, we discussed how the emission, manipulation, and detection of SWs are the key elements of magnonics. Optically, few experiments have used used GHz repetition rate fs laser pulses to emit sustained SWs [15, 16]. These measurements on insulating doped-YIG films with thicknesses close to several microns and spot sizes up to 10 μm are impractical for shrinking the size of magnonic devices and integrating them with conventional electronics. Although the pioneering works are commendable, they raise a number of intriguing questions that we would like to address: First, can GHz repetition rate fs-lasers be used to efficiently excite continuous SWs in metallic thin films, which are easily integrable in CMOS based devices? Second, in contrast with TR-MOKE, can a time-averaged technique such as BLS be used? Third, is it possible to excite both propagating and localized spin wave modes? Finally, how does the dependence of the SW amplitude on pump power look? In this section, we take a look at the results that answer these questions.

2.2.1 *k*–vector selective spin wave emission

The typical field-dependent thermal magnon spectrum for a 20 nm permalloy thin film on a sapphire substrate with a dielectric capping layer, in the presence of an oblique field, follows the Kittel-like curve given by Eq. 1.6. Since BLS is an extremely sensitive technique, we can easily measure the broadband FMR spectrum of NiFe above the spin wave band gap containing a wide range of wavevectors. However, since we are focusing the light down to the diffraction limit, in order to increase the spatial resolution, we are limited both in terms of the range of the wavevector and its resolution. With a 0.7 N.A. objective, we achieved a maximum cone angle of 49° for the light focused on the sample. This corresponds to a maximum k-vector (k_{max}) of the SW detectable using this setup of 17.8 rad/μm, or a minimum wavelength (λ_{min}) of 350 nm. Figure2.3 (**a**) shows the thermal magnon spectrum with respect to the applied field strength ($\boldsymbol{H}$) with the pump laser switched off (0 mJ/cm^2). The solid white line is the theoretically calculated FMR frequency as a function of field, which coincides well with the onset of the BLS signal. The dotted line represents the calculated wavevector cut-off. On exciting the sample with the high-repetition rate pulsed laser (pump fluence of 1.8 mJ/cm^2) and probing

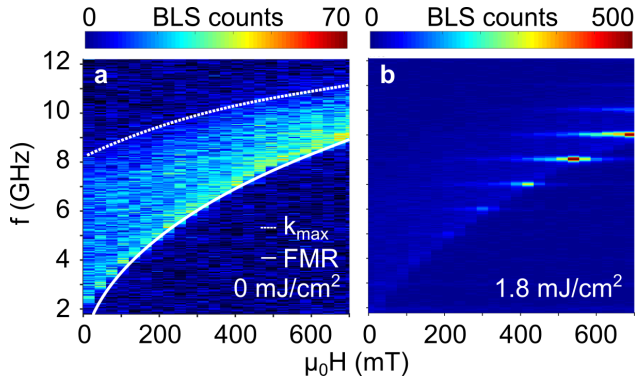

Figure 2.3: **a**. Thermal magnon spectrum measured using BLS microscopy (without pulsed excitation), showing the onset of FMR frequency and the maximum k-vector cut-off limits calculated theoretically. **b**. With a GHz repitition-rate laser to pump the sample at a fluence of 1.8 mJ/cm^2, we can observe strong enhancement of thermal modes with frequencies matching the harmonics of the pulsed laser [17].

the same spot as the pump, we observe a strong enhancement of the SW modes that match the harmonics of the repetition rate of the fs-laser, as shown in Figure 2.3 (**b**). The strongest harmonics are an order of magnitude greater than the thermal magnon signal at the same frequency. By tuning the strength of the applied field, we can choose to coherently amplify specific wavevectors of the broadband SW regime. It can also be observed that specific modes lying in the SW band gap can be amplified using femtosecond laser pulses. Later we will investigate the propagating or localized characteristics of these different modes.

2.2.2 Dependence of SW amplitude on the power of the pump laser

The energy transferred by a fs-laser pulse to a metal instantaneously creates an ensemble of hot electrons, which rapidly thermalizes at an elevated electron temperature, dissipating heat into the spin and lattice systems, as described in Sec. 1.1.4. The system then relaxes by emitting SWs in the picosecond timescale. To determine the effect of laser pump power on SW amplitude, we plotted the BLS spectrum at five different average powers of the pump laser (Fig. 2.4 **a**). At 0 mW, only the thermal magnon spectrum is seen. The signal in the SW band gap is just the dark-field counts of the detector in the interferometer. At around 8 GHz, the onset of the broadband FMR signal can be seen. Enhancement of the 8 and 9 GHz harmonic modes appears at 5 mW average pump power. At higher powers, we observe a nonlinear increase in the SW amplitude of the 7, 8, 9 and 10 GHz modes, while the other modes are not much enhanced. In Figure 2.4 **b** & **c**, it can be seen that most of the modes excited at higher powers are localized to the pump spot, while the

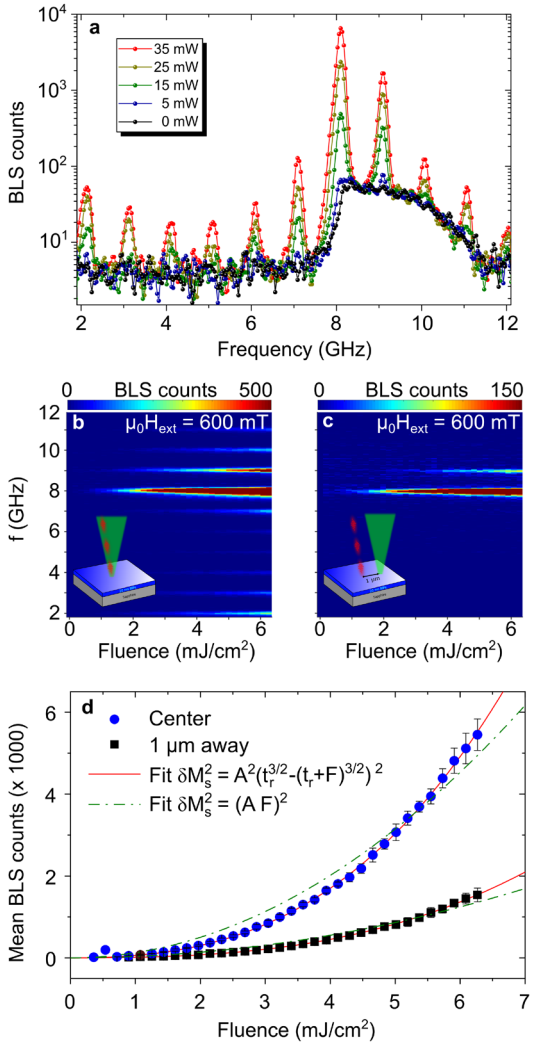

Figure 2.4: **a**. Spectra for different laser pump powers at 600 mT applied field. **b**. A color plot of the SW amplitude vs. pump fluence at the center of the pump spot and **c**. 1 μm away. **d**. Plot of mean BLS counts at the center and 1 μm away from the pump spot following Bloch's $T^{3/2}$ law (solid red line). The dash–dotted green line represents a less good parabolic fit [17].

modes at 8 and 9 GHz are propagating away from the pump region. While the signal at the center of the pump region may be slightly contaminated by nonlinear optical phenomenon, such as four-wave mixing, the signal away from the center is purely magnetic. The temperature dependence of magnetization should follow Bloch's $T^{3/2}$ law.

$$\delta M_s = A\left(t_r^{3/2} - (t_r + F)^{3/2}\right) \tag{2.1}$$

where F is the laser fluence, and A and t_r are coefficients defined by the magnetization $M_s(T = 0)$, at Curie and room temperatures, and the heating efficiency of the laser. As the SW amplitude should be linear in the demagnetization pulse (δM_s) and the BLS signal should be proportional to the square of the SW amplitude, the BLS counts can be fit with the square of Eq. 2.1 to match the experimental data. In comparison to the perfect fit shown by the solid red line in Figure 2.4 **d**, the green dash–dotted line (a parabolic fit function) deviates significantly from the experimental data.

2.2.3 Propagation characteristics

Using a high resolution microscope and TFPI, we have directly mapped the SW amplitude of all the modes simultaneously with high precision. A 2D raster scan was performed on 20 nm thick NiFe film, isotropic in the plane. We systematically altered the relative spacing between the pump and the probe spots to reconstruct the SW amplitude map. As shown previously at 600 mT applied field, only the 8 and 9 GHz modes propagated in the direction perpendicular to the in-plane component of the applied field. This corresponds to Damon–Eschbach SWs. Figure 2.5 **a** plots the SW amplitude of all harmonic modes as a function of the linear displacement between the pump and the probe. The modes from 2-7 GHz and above 10 GHz are mostly localized. The 8 GHz mode propagates up to 4 μm on either side, while the observed propagation length for 9 GHz in the same direction is reduced to about 2 μm. To calculate the SW decay length, we extracted the amplitude by performing a multiple Lorentzian peak fit for indivdual spectra at each point on the sample and plotted the log (BLS counts) as a function of the relative distance between the pump and probe (Fig. 2.5 **b**). By fitting the profiles to an exponential decay function of the form $\exp(-2x/\xi)$, where ξ is the SW propagation length, we obtain $\xi = 1.85$ μm. It is worth noting that the SW decay rate, or the damping constant, remains the same for all pump powers.

The 2D raster scan was performed for two different angles of H_{in}. Figure 2.5 **c-f** are the spatial profiles of the SW amplitude for the 7, 8, 9, and 10 GHz modes with H_{in} in the horizontal direction. The 7 and 10 GHz modes, which are below and well above the ferromagnetic resonance frequency, are localized to the pump region. The limitations in detecting high wavevector SWs might be the reason for not being able to observe its propagating characteristics. The 8 GHz mode, which matches the FMR frequency at 600 mT applied field, shows strong propagation in the direction perpendicular to H_{in}. This corresponds to the Damon–Eschbach SW dispersion relation. For the 9 GHz mode, which is a higher wavevector SW, we can observe subtle mode

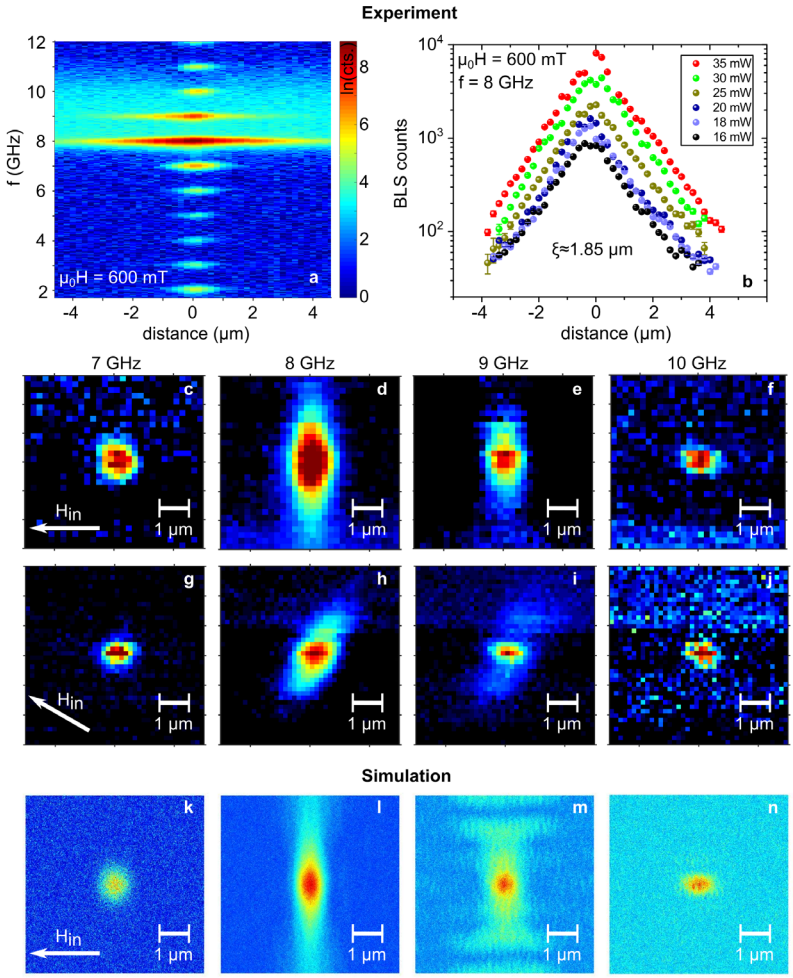

Figure 2.5: **a**. Linear profile of SW amplitude for different modes at 600 mT applied field. **b**. Amplitude of the Lorentzian peak fit data extracted for 8 GHz mode showing exponential decay for different pump powers. Extracted decay length was 1.85 μm **c-f**. 2D SW amplitude maps for four different modes at 600 mT applied field with in-plane component horizontal and **g-j**, rotated by 30°. **k-n**. Simulated area maps of the SW amplitude for 7, 8, 9, and 10 GHz modes at 600 mT applied field [17].

Parameter	Value
Saturation magnetization (M_s)	781.75 kA/m
Exchange stiffness (A_{ex})	11.3 pJ/m
Damping constant (α)	0.01
Field strength ($\mu_0 H$)	600 mT
OOP angle	82°
Pump region (diameter)	800 nm

Table 2.1: Experimental parameters used in the micromagnetic simulation.

spreading. Further investigation into high wavevector SWs will be dealt with in the sections ahead. By rotating the in-plane component of the applied field by 30°, we can observe (Figure 2.5 **g-j**) that the direction of propagation is also rotated by the same angle. This gives us control over the direction of SW emission, which is vital in magnonic and spintronic devices.

2.2.4 Micromagnetic simulations

Micromagnetic simulations were performed on a 5.12×5.12 μm^2 permalloy film of 20 nm thickness using Mumax3 [99]. To avoid the effects of finite size, periodic boundary conditions were applied. The experimental parameters used are given in Table 2.1. To recreate the effect of the pump laser used in the experiment, we implemented instantaneous quenching of the magnetic moments followed by a slower recovery, where the moments relax back to their equilibrium. A Gaussian beam profile with a FWHM of 800 nm, as in the experiment, was chosen as the area of excitation. The sequence was repeated at a clock frequency of 1 GHz by adding or subtracting the demagnetization tensor corresponding to the magnetization state at both the demagnetized and the recovered states. The number of magnons (N) per unit volume (density of magnetic moments carried by spin waves), at a certain frequency ω, was extracted from the results of simulations using Eq.(S19) in [100],

$$N(\omega) = \frac{M_s}{2\mu_B} \mathbf{m}^*(\omega) \cdot [\mathbf{m}_0 \times \mathbf{m}(\omega)] \,, \tag{2.2}$$

where $\mathbf{m_0}$ is a unit vector in the direction of the equilibrium magnetization, and $\mathbf{m}(\omega)$ the dynamic magnetization in Fourier space. Our micromagnetic simulations show almost perfect quadratic dependence of the magnon population at 8 GHz on the induced demagnetization δM.

The simulation results agree well with the experimentally measured spatial profiles of the different spin wave modes. The 2D maps of the SW amplitude in Figure 2.5 **k-n** correspond to the theoretically calculated 7, 8, 9, and 10 GHz modes. As described previously, the 8 GHz mode, whose frequency matches with the FMR frequency of the system, propagates the most in the direction perpendicular to H_{in}.

2.3 Spin Wave Caustics

Manuscript III: A point source in an isotropic material radiates energy uniformly in all directions. In contrast, an anisotropic medium has different directions for phase and group velocities. The energy from a point source may thus be focused in specific directions. These focused energy beams, called caustics, were first observed in optics, where envelopes of light rays are formed by refraction and reflection from curved surfaces [101, 102]. This phenomenon has found application in studies of stress intensity factors in transparent materials using the shadow optical method [103–106]. Self-focusing of propagating phonons was observed in anisotropic continuous media as a result of the creation of nondiffractive beams [107–109]. In dark matter physics, observables such as gravitational lensing [110] and annihilation radiation [111] are known to have had a positive impact due to caustics.

The self-focusing of SWs has been studied in detail theoretically [112–114], and also experimentally demonstrated in structured YIG films [115–117], where SWs are induced by a microwave antenna into a narrow waveguide, which opens into a broader magnetic film area at the other end. In such cases, the point at which the SW waveguide meets the extended film acts as a point source, leading to caustic patterns. Similar effects have also been observed in structured NiFe thin films [118]. Recently, several demonstrations of SW signal splitters [119] have been shown, using sample geometries similar to the one mentioned above.

A major drawback of the above method is the necessity of fabricating micro-structures, which confines the SW point source to a single position and allows less freedom to move around the sample. We can alleviate this problem by using an optically manifested SW point source that can produce caustic SW beams. Here we use a femtosecond laser focused down to the diffraction limit, acting as an ideal point source. The GHz repetition rate of the excitation is faster than the energy dissipation of the magnons, thus providing a continuous source of SWs. Finally, a BLS microscope allows us to measure all the SW modes with different wavevectors simultaneously, with good spatial resolution for estimating the angle between the caustic beam and the in-plane component of the applied field.

2.3.1 X-shaped propagation of SWs

For the purpose of this study, we chose a small region between 400 and 850 mT for the three modes at 7, 8, and 9 GHz (Figure 2.6 (**S1**)). As described earlier, the maximum for each mode corresponds to that field value where the FMR frequency of the sample matches the particular repetition harmonic. At this point the propagation of SWs is strongest, is unidirectional, and is perpendicular to the direction of H_{in}. This is shown in the area maps C4, B7 and A7 (Red outline) for the 7, 8, and 9 GHz modes respectively. Let us focus on the area maps corresponding to the 8 GHz mode, which shows prominent caustic behaviour. As we increase the field strength from this point (B8-B11), the mode enters the SW band gap region, gradually becoming localized to the

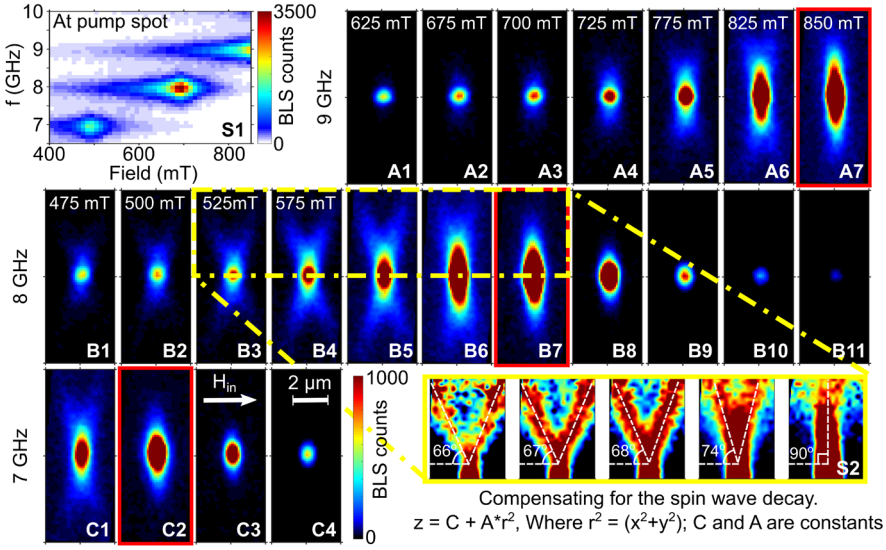

Figure 2.6: **S1:** SW amplitude as function of field and mode frequency, focusing mainly on the 7, 8, and 9 GHz modes. **A1-A7:**Area maps showing BLS counts on color scale for the 7, **B1-B11:** 8, and **C1-C4:** 9 GHz modes at various field strengths. Maps **B3-B7** were replotted by compensating for the spin wave decay in **S2**. Estimates of the caustic beam angle *w.r.t* the direction of H_{in} are mentioned.

pump spot and eventually vanishing. With decreasing field however, the mode is pushed into the high wavevector region (B3-B6), thus changing the wavevector and consequently the spatial profile of the particular mode. We clearly see X-shaped patterns where the propagation angle *w.r.t* $\mathbf{H_{in}}$ decreases with field. The box highlighted in yellow shows BLS intensity of decay-compensated amplitude of the spin wave, for better visibility of the caustic beams. This is done by multiplying the intensity at each point by square of the distance form the pump spot. The dashed white lines are visual guides giving an estimation of the propagation angle. The angle changes from ≈66° for B3 to 74° for B6. The weaker SW intensity in subplots B1 and B2 of Figure 2.6 are due the decreasing efficiency of both the excitation and the BLS detection at higher wavevectors. Similar caustic behaviour can be seen for the 7 and 9 GHz modes.

2.3.2 Isofrequency curves and theoretical calculation of propagation angles

To calculate the propagation angle of the SWs, we need to first plot the isofrequency curves for the corresponding SW modes. Consider a point source with characteristic size r in a continuous medium with anisotropic properties. This can emit waves with all wavevectors ($\mathbf{k}$) up to $\sim 1/r$ and group velocities ($\mathbf{v}_{gr}$), defined by a dispersion relation as $\mathbf{v}_{gr} = 2\pi\nabla f(\mathbf{k})$. If the surface of the

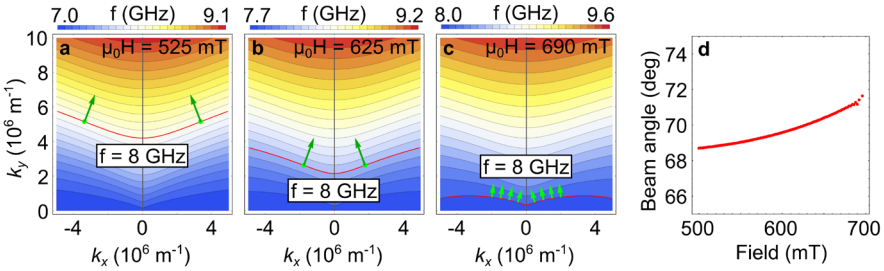

Figure 2.7: a)–c) Isofrequency curves for 8 GHz at different applied fields. The caustic points defined by Eq. (4) are shown by green dots, while the directions of the caustic beams are indicated by the darker arrows. c) shows the preferred direction of the emitted SWs for high field, where there is no caustic X-shaped pattern; d) Caustic beam angle vs. applied magnetic field.

emitted frequency $f_0(\mathbf{k})$ (isofrequency surface) contains "flat" regions, then all waves with wavevectors in this region will have the same direction of $\mathbf{v}_{gr}$, leading to the formation of high-intensity unidirectional beams [120, 121]. A detailed theoretical analysis of caustic SW beams in a thin magnetic film is presented in [117], which we follow here.

The magnon dispersion relation, following a simplified version of Eq. (45) from [122] for SWs in the plane of a thin magnetic film, is:

$$f = \frac{\gamma\mu_0}{2\pi}\sqrt{(H_{int} + M_s l_{ex}^2 k^2)(H_{int} + M_s l_{ex}^2 k^2 + M_s F_0)},$$
$$F_0 = P_0 + \cos^2\theta_{int}[1 - P_0(1 + \cos^2\phi) + \\ + M_s(P_0(1 - P_0)\sin^2\phi)/(H_{int} + M_s l_{ex}^2 k^2)],$$

where $P_0 = 1 - (1 - \exp(-kL))$, $l_{ex} = \sqrt{2A/(\mu_0 M_s^2)}$, and H_{int} and θ_{int} define the strength and OOP angle of the internal field; these can be found using the solution to the magnetostatic problem mentioned in Eq. 1.7 in Sec. 1.1.1.

The parameters mentioned in Tab. 2.1 are used to calculate the isofrequency curves plotted in Figure 2.7 (**a-c**). The frequency of magnons vs. wavevector components $k_x = k\sin\phi$ and $k_y = k\cos\phi$, is shown in these contour plots. Next, we extract the isofrequency line $k_x = g(f, k_y)$ for the frequency of excitation $f = 8$ GHz, which is shown by the red line in Figure2.7. The condition for a caustic beam is represented mathematically as:

$$\partial^2 g(f, k_y)/\partial k_y^2 = 0, \tag{2.3}$$

from which we can extract the wavevectors of the caustic beams $\mathbf{k}_c$, represented by green dots on Figure 4a and 4b. The group velocities, and thus the direction of propagation of the caustic beams are perpendicular to the isofrequency line at these points, which can be written as $\pi/2 - \phi_c = \arctan(\partial g(f, k_y)/\partial k_y)$. The direction of propagation is shown by the green arrows. The propagation angle ϕ is defined by the direction between the in-plane component of the field, $\mathbf{H_{in}}$, and the wavevector, $\mathbf{k}$.

The wavevector of the caustic beam decreases with increasing field (see Fig. 2.7d), until at some point $k_x \to 0$. At this point, the condition in Eq. (2.3) can no longer be satisfied for this particular isofrequency curve and, as a consequence, the caustic beam ceases to exist. Instead, the isofrequency curve shows a nonzero second derivative everywhere, as illustrated by the green arrows in Figure 2.7c. With the given simulation parameters at $H \simeq 0.69$ T, we cannot find a solution for the caustic beam condition. For higher fields, the slope of the isofrequency curve becomes very small. Due to the symmetry of the propagation direction for positive and negative k_x, the SWs are emitted primarily in the y direction, as we observed above from the BLS spatial maps.

In conclusion, we have described a unique experimental femto-BLS technique that combines a pump setup consisting of a GHz repetition rate femtosecond pulsed laser with a sensitive BLS microscope as the probe. The combined technique is quite fast and sensitive, and can be used to excite and detect sustained coherent SWs. Finally we have studied various properties of the excited SWs, such as field dependence, power dependence, and propagation characteristics. A thorough study of caustic propagation of SWs was also conducted, making use of the versatility of the measurement technique.

3

Spin Hall nano-oscillator arrays

Nano-oscillators based on STT are unique devices that have potential applications in future CMOS compatible communication devices. In this chapter we will take a look into nano-constriction based SHNOs that are easily tunable, and have been studied extensively [123–130]. The nonlinearity in the system is known to aid mutual synchronization of several closely spaced oscillators. Early proposals for synchronization of multiple oscillators were suggested to improve output power and signal coherence in STNOs and SHNOs [131, 132] as compared to the conventional microwave oscillators. In STNOs, mutual synchronization via propagating spin waves has been demonstrated [39, 133–135]. Mutual synchronization of SHNOs have been studied extensively in 1-dimensional chains [63]. Up to 21 oscillators in a single chain have been successfully synchronized until now.

In this chapter, we target the characterization of 2D arrays of SHNOs. Multiple factors, such as easier fabrication procedures, enhanced nonlinearity, and easy optical access to individual oscillators, make SHNO arrays more practical than STNO arrays. However, a large parameter space in terms of device layout, bias current, field magnitude and angle and temperature encourages a detailed analysis of such devices. The phenomenon of synchronization has been observed in various instances in nature, starting from fireflies and circadian rhythms to hippocampal activity in the nervous system [136–138]. Although technological implementations of the synchronization phenomena have been achieved using arrays of micro-mechanical oscillators, Josephson junctions or STNOs [39, 63, 139–143], the power consumption and size of these devices are larger than the natural counterparts. We show here a direction towards achieving potential neuromorphic computers and IMs using spin Hall nano-oscillators and the phenomenon of synchronization along with phase locking using external microwave signals. As part of this thesis we focus mostly on the optical detection of magnetization dynamics for various operating conditions of the oscillators.

The detailed fabrication procedure of a single SHNO is given in Sec. 1.2.1. For a SHNO array the design layout is drawn carefully to match the mode-expansion properties of localized SW mode [81] for a given set of experimental

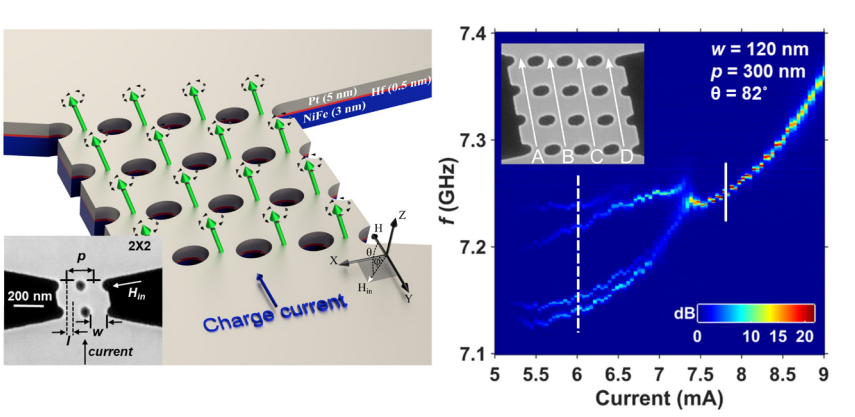

Figure 3.1: **a.** Schematic representation of a 4×4 array of SHNOs. The green arrows on top of the oscillators represents precessing magnetic moments. The inset contains an SEM image of a 2×2 array showing all the design parameters (w,p and l. **b.** power spectral density (PSD) map of bias current vs frequency at 680 mT applield field. The solid line represents a synchronized state and the dashed line represents unsynchronized state [144].

conditions. Each array was defined by three important parameters: i) constriction width (w), ii) pitch size (p) which is the distance between the center to center distance between adjacent SHNOs in a row or the distance between two adjacent rows, and iii) lateral shift (l) which is the lateral shift between two adjacent SHNOs in a column. Different values of w and p were chosen to control the coupling strength between the oscillators and l was chosen accordingly to have maximum overlap of the SW modes. Arrays ranging from 2×2 to 10×10 oscillators were fabricated with 4 different combinations of (w,p): (50,100), (80,140), (120,200), and (120,300). Fig. 3.1 **a** shows the layout of a 4×4 array of SHNOs with the coordinate system showing the direction of charge current and field angle (both IP and OOP). A tri-layer of NiFe(3nm)/Hf(0.5nm)/Pt(5nm) (color coded as blue, red and gray respectively) was used on high resistivity silicon substrate. The inset of Fig. 3.1 shows an SEM image of a 2×2 array depicting the width(w), pitch size(p) and lateral shift(l).

3.1 Mutual synchronization of arrays

3.1.1 Electrical measurements

Manuscript IV: Basic characterization of the arrays was performed by acquiring the electrical spectrum by sweeping the bias current over a range of values. The applied field strength was fixed to be 680 mT at an angle of 76° OOP and 30° IP. Most arrays with smaller pitch size and width were found to achieve synchronized state quite easily. However, for the largest pitch size and width, only 2×2 arrays were found to achieve a robust synchronized state. For

larger arrays the coupling is weaker and the oscillators are not synchronized anymore.

Here we present a detailed electrical and optical analysis for a 4×4 array of SHNOs. With 680 mT applied field at OOP angle $\theta = 82°$ we could obtain a power spectral density (PSD) measurement as shown in Fig. 3.1 **b**. We can clearly see 4 different modes from the 16 oscillators at low current, which suggest that either the rows (horizontal) or the columns (vertical) are synchronized. It is noteworthy that at higher OOP angles, the mode expansion is stronger as predicted by Ref. [81]. This aides the synchronization of the SHNOs in the direction of the current. As we go to higher currents, the 4 synchronized chains combine to form one synchronized mode with higher output power and lower linewidth.

3.1.2 Optical measurements

To better discern the spatial features of the different modes, we performed a raster scan of the largest 4×4 array (w = 120 nm; p = 300 nm) using BLS microscopy. The operating points were chosen such that unsynchronized and a synchronized modes are studied to observe their contrasting behaviour. At I = 6 mA; H = 680 mT as marked by the dashed line in Fig. 3.1 **b** there are 4 different modes which are most likely the 4 chains along the direction of current that are synchronized. The two lower modes are separated by around 20 MHz and the two upper modes follow a similar behaviour. The upper and lower modes are however separated by around 100 MHz which is close to the frequency resolution of the BLS microscope. A complete robust synchronization is seen at I = 7.8 mA; H = 680 mT as marked by the solid line Fig. 3.1 **b**. The measured electrical output power at this point is much higher than the unsynchronized output.

Several experimental challenges need to be overcome to perform a reasonably good optical measurement. First, the optical resolution of the instrument is close to 300 nm which is slightly larger than the pitch size of the 4×4 array. A measurement with 60 nm step size between two consecutive points provides best possible image. However, due to minor mechanical drifts and low probe power during the measurement the closest SHNOs cannot be resolved very well. Second, the substrate used in the measurement is a high resistive silicon substrate which shows a photovoltaic effect. Additionally, since the sample is metallic, heating of the sample with laser irradiation is unavoidable. Hence, using higher laser power to obtain larger signal-to-noise ratio is not favourable. Laser heating also breaks the synchronization. An optimal power of 500 μW was used to minimize the laser induced effects as well as improving the optical signal. Third challenge is the aging of the devices. Since each area map takes slightly longer than 6 hours with optimal measurement conditions, the speed of measurement directly affects the quality of the image and the lifetime of the devices.

Fig 3.2 shows the area maps obtained for linear mode (or FMR), and other non-linear auto-oscillation (AO) modes discussed earlier. The area map of broadband FMR mode which is significantly weaker than the AO modes is

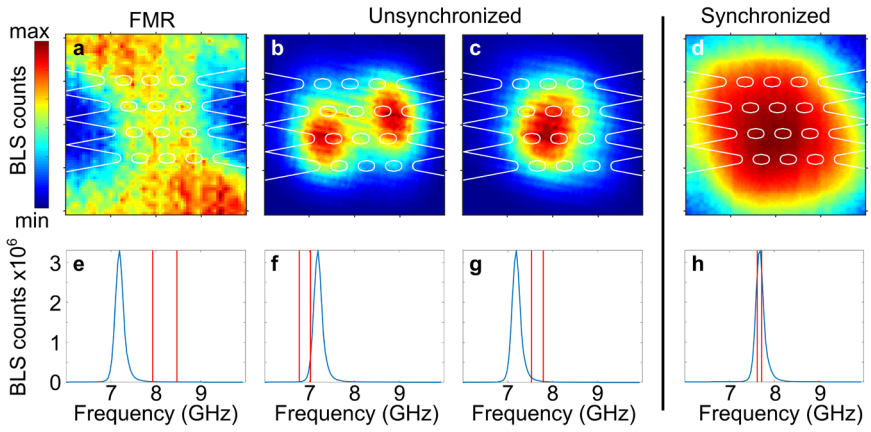

Figure 3.2: **a-d**. Represents 2D maps of magnetization dynamics for 4×4 array of SHNOs for different modes **a.** FMR, **b & c.** unsynchronized mode corresponding to the dashed line in Fig. 3.1(**b**), **d.** synchronized mode corresponding to the solid line in 3.1(**b**) plotted in log scale. **e-h**. shows the BLS spectrum with the red lines showing the range of frequencies chosen for the corresponding area map above it.

shown in Fig 3.2 **a** The map is plotted for the frequency region denoted in Fig 3.2 **e** Since the measurements for synchronized and unsynchronized AO modes are done along the same 2D grid with active stabilization of the stage using image recognition, we used the FMR map to fix the outline of the sample (in white lines) on the area map approximately. In Fig 3.2 **b** & **c**, two parts of the unsynchronized regime are plotted separately. The lower part of the spectrum, which corresponds to the lower modes in Fig. 3.1 **b** is localized around the outer most chains A and D in the device, while the upper modes are located closer to the center where the two central chains B and C are. Since the frequency resolution of the BLS microscope is close to 100 MHz, the different modes cannot be resolved well in the spectrum shown in Fig 3.2 **f** & **g** For the synchronized mode, operating at higher mode frequency, all the oscillators are operating at a single frequency. The BLS map in Fig 3.2 **d** plotted on a logarithmic color scale shows an expanded mode clearly encompassing all the oscillators. The counts present in the holes in the sample are due to the overlapping measurements, since we use a 350 nm diameter beam with a 60 nm step size for scanning. From the results discussed above we can get the first indication that the SHNOs along the chains A, B, C & D synchronize first and the different chains synchronize at higher currents.

For a more conclusive proof that the SHNOs in a chain synchronize first we performed line scans along the row and column of a 4×4 array as shown in Figs.3.3 **c** and **e**, respectively. The corresponding BLS maps are shown in Fig.3.3 **b**, and **d**. The operating point was chose such that 4 AO modes are shown as in Fig.3.3 **a**. Each mode (1,2,3 & 4) corresponds to a synchronized chain (A,B,C,& D). The BLS maps along the row (Fig.3.3 **b**) shows a change

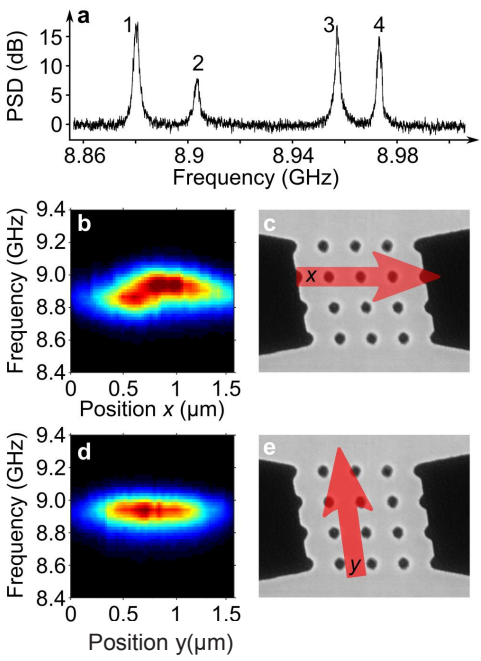

Figure 3.3: **a.** PSD plot of a 4×4 array with $(w, p) = (120, 300)$. **b.** The BLS map of the line scan along the row **c**. as denoted by the red arrow in the horizontal direction. **d.** BLS map of the line scan along the column **e.** as denoted by the arrow in the vertical direction [144].

in the mode frequency as the laser is scanned across the oscillators. This immediately confirms that the oscillators in the row are not synchronized. As we scan along a single chain, the BLS map (Fig.3.3 **d**) shows a constant operating frequency throughout, which suggests that the oscillators are synchronized. In conclusion the coupling along the chains (exchange + dipolar) is stronger compared to the coupling between the chains (only dipolar), which is likely also why the arrays with larger pitch size fail to synchronize.

3.2 Neuromorphics using SHNO arrays

Neural activity is one of the fastest, most efficient processes occurring in a natural system. To mimic the neural activity artificially is a challenging task. Several theoretical proposals have been made around the turn of 21st century to use nonlinear oscillators [145–147] to design processors capable of handling neuromorphic computing. A proof of concept of the theoretical study has been demonstrated using memristors [148], superconducting oscillators [149] and

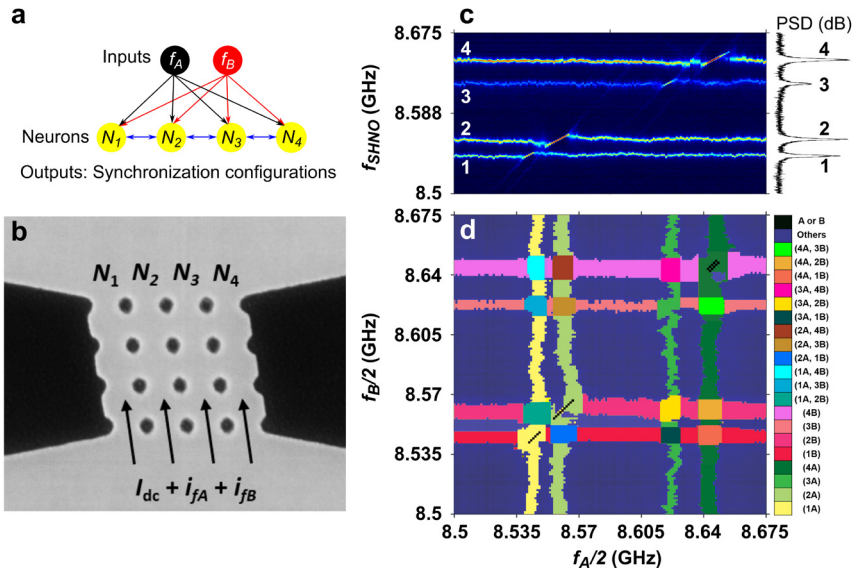

Figure 3.4: **a.** Layout of different synchronization configurations (N_{1-4}) with inputs f_A and f_B for the **b.** 4×4 array showing the synchronized chains (N_{1-4}). **c.** PSD plot showing injection locked regions. **d.** The synchronization map along with the color coded configurations [144].

very recently using magnetic tunnel junction based STNOs [64, 150]. Ref. [64] deals with reservoir computing using 4 vortex oscillators connected electrically in series. The device was used to recognize 7 different vowels spoken by 35 speakers. A linear combination of 12 frequency components in the spoken vowels was used to map the input frequencies into two RF signals injected by an antenna close to the STNO chain. When the frequency of the RF inputs are close to the natural frequency of the STNOs, they are phase-locked to one or both of the input signals. A 2D-synchronization map was created, where specific synchronized regions in the map corresponds to specific vowels.

Due to the weak coupling between the STNOs and practical limitation of creating a large number of wire-bonded STNOs, scaling up such a device is quite challenging. In this work, we attempted to recreate the synchronization map using our SHNO arrays, discussed in detail in Sec. 3.1. We used a 4×4 oscillator array to create the synchronization map where the the 4 synchronized chains N_{1-4} represent 4 neurons operating at 4 different frequencies as shown in Fig. 3.4 **c**. Two microwave signals, at frequency f_A and f_B (close to twice the SHNO frequency f_{SHNO}), were generated using two R&S SMB100A sources, then combined using a mixer and finally fed into a circulator connected to the prove to the device. By sweeping the frequency f_A in a certain range, we first observe that each synchronized chain gets phase-locked at a specific range as shown in Fig. 3.4 **c**. The 2D synchronization map in Fig. 3.4 **d** is then reproduced by sweeping both f_A and f_B. The color code represents different configurations where the numbers represent the active chain phase-locked with

the input signal represented by the letter. A total of 20 distinct regions are mapped. Our demonstration indicates the possibility of carrying out reservoir computing similar to Ref. [64] at frequencies up to 8.7 GHz which is about 25 times faster than the STNOs.

The coupling between the oscillators in the rows and columns play an important role in the synchronization of the two-dimensional network of interacting oscillators. Almost all proposals for using oscillator arrays for different computation paradigms [139, 151–160] require a strong coupling between these oscillators. A strong exchange and dipolar coupling that are tunable by tuning the current and field applied in our SHNO array makes them notable candidates to be used in neural networks. One such application is to use the SHNO network based as Ising Machines to solve combinatorial optimization problems, which we will look into in the next section.

3.3 A SHNO based Ising machine

Manuscript V: A large class of problems in computer science, known as non-deterministic polynomial time (NP) problems, have an exponentially increasing computation time with the number of variables. These problems manifest themselves in real life scenarios such as business operations, manufacturing and research, protein folding, image recognition, maximizing influence in a social network, *et cetera*. A set of these problems are called combinatorial optimization problems. Computing such problems using von-Neumann architectures is both time and power consuming. Natural computing is one of the alternative computing schemes where we can map the problem onto a physical system and the solution is provided by the ground state energy of the system. Many proposals for hardware that falls in the realm of natural computing have been put forward.

Ising machines (IMs) are one such class of hardware, where the node interactions (coupling) can be described by an Ising Hamiltonian and the system relaxes into its ground state based on the coupling strength between the nodes. The ground state then gives the solution to the problem which can be achieved much faster in an IM than a traditional von-neumann computer. Given the efficiency of an IM in solving combinatorial optimization problems, multiple recent hardware architecture have been demonstrated using quantum annealers [161, 162], CMOS annealers [163], nano-magnet network arrays [164], electronic oscillators [151, 165], and laser networks [166–168]. D-Wave one (Rainer) is the first quantum annealing processor implementing the Ising model using 128 qbits. Later, its succesor D-wave 2000Q with 2048 qbits was used to solve large scale Max-Cut problems. However, the requirement of cryogenic facilities makes it inefficient both in terms of power consumption and cost. Coherent Ising machines (CIM) using optical parametric oscillators (OPO) [168–170] are room temperature alternatives. However, they are not scalable in terms of size since CIMs require large infrastructure such as an optical table, long optical fibres and are also hard to tune to different operating frequencies. In 2018 Fujitsu announced its state-of-the-art field-programmable digital array

(FPGA) with 8192 simulated qbits in a network. The superior connectivity in this implementation makes it possible to deal with real-scale combinatorial optimization problems. The main drawback however is the use of von Neumann computing paradigm which is brute force computing algorithm rather than using the nature of the physical system. It will therefore not scale well to much larger sizes.

Recently non-linear oscillator-based IMs have been proposed [171] where a network of coupled oscillators are used. The phase dynamics in such a system minimizes the Lyapunaov function, which is a scalar function that serves as a measure of the network stability. By pumping the network with a microwave signal close to the second-harmonic frequency of the oscillator we can injection lock the oscillators with binarized phase 0 or π. Under second-harmonic injection locking (SHIL), the Lyapunov function translates into Ising Hamiltonian and the network of non-linear oscillators can operate as an IM. In Ref. [172] the authors demonstrate a prototype of 240 resistively coupled oscillators achieving an unprecedented computation time of 1 ms for an operating frequency of 1 MHz and consuming a meager 5 W of power. The possibility of achieving significant increase in the processing speed and integrating a larger number of oscillators is now limited by the Moore's law for CMOS based oscillators. Our network of SHNOs, as explained in the previous sections, show robust synchronization properties within the network as well as to external microwave sources. The strong, easily-tunable coupling between the oscillators and GHz operating frequencies makes SHNO arrays an important candidate for IM architectures.

We were able to show binarization of the phase states in a network of 1×2 and 2×2 SHNO arrays using electrical and optical measurements. We used SHIL technique described in Sec. 3.2 by sweeping the power and frequency of the injected signal and detecting the signal electrically using a spectrum analyser More details about the electrical measurements can be found in *Manuscript V*. In order to distinguish the phases of individual oscillators in the network, we used a phase-resolved BLS miscroscope. In this experiment, two phase locked signal generators operating at *f* and *2f*, where *f* is close to oscillator frequency, are used in parallel to modulate the light using an electro-optical modulator (EOM) and to parametrically pump the SHNO array respectively. The inelastically scattered light is carries the phase information of the oscillator and the polarization is rotated by 90°. The phase and the polarization of the elastically scattered light is unaltered. By mixing the two beams using a high extinction ratio polarizer and setting the angle such that equal intensity of the elastic and inelastic light beam we can produce interference patterns whose intensity translates directly into the phase of the oscillator. The combined light beam is studied using TFPI.

By measuring the electrical output of the SHNO after parametrically pumping the 1×2 array we observed clear hopping between two states of power. Fig. 3.5 **a** shows the layout of the 1×2 array where the green dashed line with an arrow represents the scan direction passing through the center of SHNO 1 and SHNO 2. In Fig. 3.5 **b** & **c** the two SHNOs are out-of-phase by 180°. Practically the two subfigures provide the same information. However,

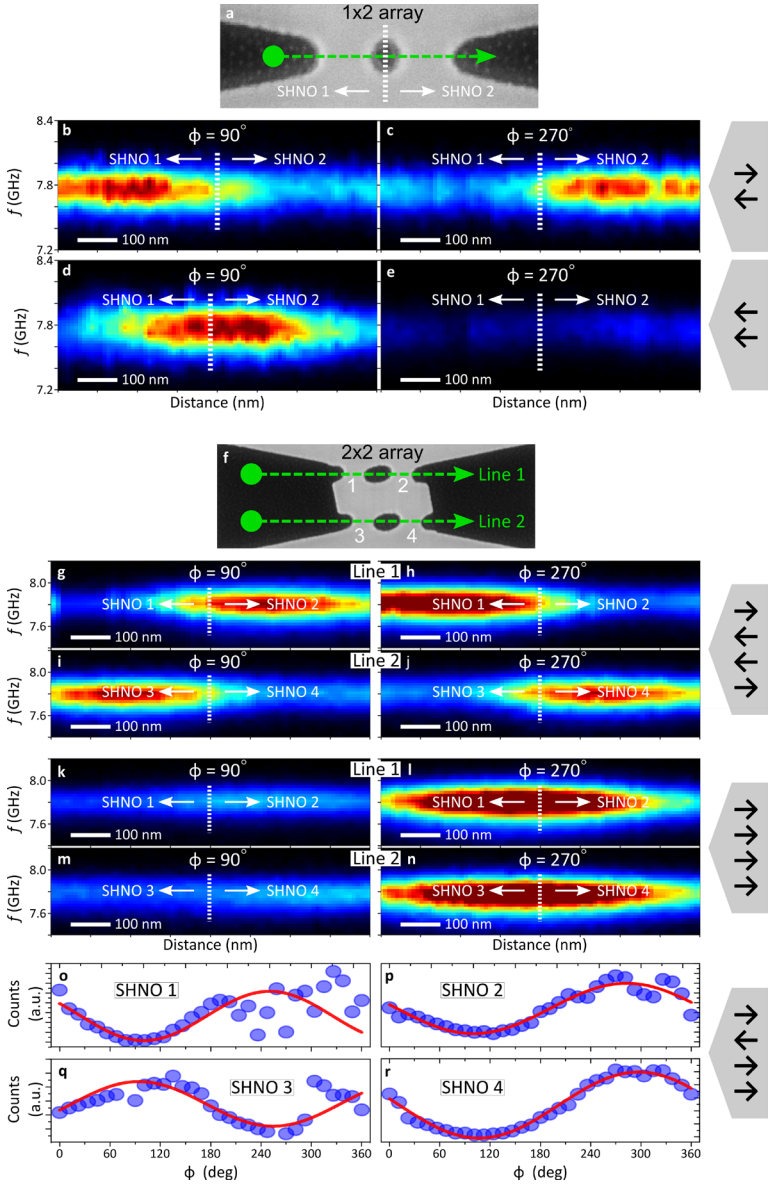

Figure 3.5: **a.** Layout of 1×2 array of SHNOs showing a dashed green line representing the scan direction along the sample. **b-e.** Line scan of BLS counts for a 1×2 array with a given phase relation (ϕ) between the light and the microwave injection signal. **f.** Layout of a 2×2 array of SHNOs. **g-j.** Array is in a low power state where the oscillators are out of phase by π. In **k-n.** all the oscillators are in-phase representing a strong output. **o-r.** are extracts of the peak amplitude of the individual spectra representing the unstable intermediate state with three oscillators in-phase and one out-of-phase by 180°.

contrasting figures at $\phi = 90°$ and $\phi = 180°$ prove that the oscillators are almost exactly π out-of-phase. Fig. 3.5 **d** & **e** represent the high power state where the two oscillators are in-phase. The BLS line scans represent equal intensity of the output for both SHNOs in this case. For $\phi = 90°$ the phase of the oscillator matches with that of the light and hence a strong signal is detected due to constructive interference. At $\phi = 270°$ the phase of the oscillator and light differ by π and destructive interference causes close to zero BLS counts. The minimum signal that is seen is due to a small error in the polarization angle.

For 2×2 arrays we observed three different amplitudes of the electrical output: *i)* High state, *ii)* low state, and *iii)* intermediate state. The high and the low states are quite stable due to low susceptibility to external disturbances and high coupling strengths. However, the intermediate state is slightly unstable and the study of the same using BLS microscopy that requires longer measurement times is harder. The different states are set by adjusting the power of the injected microwave signal, magnetic field strength as well as the bias current applied on the SHNO array. In Fig. 3.5 **g** & **j**, the low state where oscillators 1 and 4 (the oscillator numbers are shown in Fig. 3.5 **f**) are in phase and oscillators 2 and 3 are in phase but 180° out of phase with 1 and 4 represented by $\langle\downarrow\uparrow\uparrow\downarrow\rangle$ can be seen. Alternatively one can also observe energetically degenerate states which can be represented by $\langle\uparrow\uparrow\downarrow\downarrow\rangle$ or $\langle\uparrow\downarrow\uparrow\downarrow\rangle$. At the high state, all the oscillators are operating in phase $\langle\uparrow\uparrow\uparrow\uparrow\rangle$ thus giving a strong electrical output. An alternative measurement technique is to measure the BLS counts above each individual constriction by sweeping through the phase (ϕ) of the light. The plots for these measurements are shown in Fig. 3.5 **o-r** The measured BLS counts is denoted by solid blue circles and the red line represents a sinusoidal fit. SHNO 1, 2, and 4 are in phase while SHNO 3 is 180° out of phase with the others. This proves that the array is in an intermediate state with the phase configuration represented by $\langle\uparrow\uparrow\downarrow\uparrow\rangle$. The intermediate state has four degenerate states and phase resolved BLS measurements allows us to identify exactly which SHNO is out-of-phase with the rest.

The above presented 2×2 SHNO array is an example of an oscillator-based IM capable of solving minimization problems. By tuning the field strength minimally, we can change the coupling strengths, consequently the phase configuration and finally the power of the electrical output in the SHNO array. These output levels can then be used to identify the different phase configurations studied using phase-BLS measurements. For simple 2×2 SHNO arrays it is easy to list all possible 2^4 solutions to the given optimization problem. In case of lager arrays such as 10×10, there are 2^{100} possible solutions which proves the computational power of IMs. The exact solution then depends on the coupling strengths which is the Ising Hamiltonian of a given problem. Controlling the individual coupling constants then becomes a key requirement to map the given problem on to the IM. Our future steps are thus focused in this direction so that a fully integrated SHNO based IM can be achieved.

Conclusions and Outlook

As a premise of this thesis, it was established that light plays an important role in both excitation and detection of non-linear magnetization dynamics. This thesis has demonstrated both aspects. First, ultrashort laser pulses with a high repetition rate was used to excite non-linear dynamics in magnetic thin films and the resulting magnetization dynamics was studied using a sensitive BLS setup capable of performing high spatial resolution measurements. Second, SHNO arrays were excited electrically to achieve synchronized auto-oscillating modes. The observed electrical output is limited in terms of getting an average output signal from all the oscillators. To understand the behaviour of individual oscillators, we performed phase and spatially resolved BLS measurements to map the mode behaviour of individual oscillators and their phase states. A proof of concept Ising Machine for possible applications using the same were also demonstrated.

As we step into the ultrafast regime of magnetization dynamics, the electronic detection mechanisms are limited in terms of speed and spatial resolution. In Chapter 1 & 2, the design of the unique all-optical pump-probe setup using pulsed and continuous wave lasers has been described in detail. We have showed that the way to overcome the low duty cycle effects of a time-averaged technique such as BLS microscopy in pump-probe techniques is to use a high-repetition rate (in GHz) femtosecond pulsed laser to achieve strong signal amplification that can be read using $\mu-$BLS. The integration of a scanning setup using a set of 4 lenses placed precisely in the conjugate planes is vital to perform 2D spatial maps of the excited magnetization dynamics. Using this setup we were able to excite sustained coherent propagating spin waves in NiFe thin films. The direction of propagation could be controlled by changing the orientation of the magnetic field. By tuning the strength of the magnetic field, we observed a caustic behaviour where the caustic angle could be tuned. Controlling the emission of spin waves using light plays an important role in magnonics. So far we have demonstrated emission of spin waves at a single spot in the sample. Further steps would be to implement spatial a light modulator to shape the laser beam at multiple spots and excite coherent spin waves in specific patterns. Spin waves also form a medium of communication between STNOs and SHNOs for synchronization. Hence studying the effects of laser induced spin waves on these devices is a necessary step forward. Implementation of plasmonic antennas to focus light below the diffraction limit is essential for technological applications where size of the device matters.

In Chapter 3, the importance of synchronization in two dimensional arrays of nano-oscillators and their application in practical non-Von Neumann

computing was described. With the ever-increasing demand for faster and smaller electronics, the study is timely and apt since SHNOs are potential alternatives that are faster, smaller and more energy efficient than CMOS based electronics. In this thesis, robust mutual synchronization of 2D arrays of SHNOs was observed, where the oscillators in the chains (along the direction of the current) are synchronized first and then the chains synchronize with each other. Using injection locking of the indivdual chains, we demonstrated as a proof of concept, that SHNO arrays can be used for neuromorphic computating. Additionally, using phase-resolved BLS measurements and second harmonic injection locking, we were able to demonstrate a SHNO based Ising Machine where the computing is done by the interacting physical system. The BLS measurements were able to distinguish all possible phase configurations in a 2×2 array of SHNOs for a given output power. Although SHNO arrays have proved to be strong candidates for alternative computing paradigms, a few drawbacks makes them not sufficient yet for applications. ***a.*** Output power of SHNO arrays are lower than their CMOS counterparts by orders of magnitude ***b.*** lack of control over individual oscillators and coupling strengths are essential to map computational problems on to physical systems, ***c.*** Use of large magnetic fields are practically inconvenient. Research addressing these challenges have already begun where perpendicular magnetic anisotropy (PMA) based layers are used to fabricate SHNOs along with an MTJ on top of each oscillator to obtain strong electrical output. Controlling the individual oscillators and coupling strengths can be done by applying voltage across the magnetic layer to control different parameters and also simply by using laser to heat the oscillator. In short, nonlinear magnetization dynamics will continue to play a vital role in various fields such as spintronics, photo-magnonics, neuromorphics, etc. Contactless emission and detection of such dynamics forms a core research area where our results demonstrate the versatility of femto-BLS microscope for its study.

Bibliography

[1] E. Beaurepaire, J.-C. Merle, A. Daunois, and J.-Y. Bigot, "*Ultrafast Spin Dynamics in Ferromagnetic Nickel*", Physical Review Letters **76**, 4250–4253 (1996).

[2] G. Ju, A. V. Nurmikko, R. F. C. Farrow, R. F. Marks, M. J. Carey, and B. A. Gurney, "*Ultrafast Time Resolved Photoinduced Magnetization Rotation in a Ferromagnetic/Antiferromagnetic Exchange Coupled System*", Physical Review Letters **82**, 3705–3708 (1999).

[3] M. van Kampen, C. Jozsa, J. T. Kohlhepp, P. LeClair, L. Lagae, W. J. M. de Jonge, and B. Koopmans, "*All-optical probe of coherent spin waves*", Physical Review Letters **88**, 227201 (2002).

[4] B. Koopmans, M. Van Kampen, J. T. Kohlhepp, and W. J. De Jonge, "*Ultrafast magneto-optics in nickel: magnetism or optics?*", Physical Review Letters **85**, 844–847 (2000).

[5] A. V. Kimel, A. Kirilyuk, A. Tsvetkov, R. V. Pisarev, and T. Rasing, "*Laser-induced ultrafast spin reorientation in the antiferromagnet TmFeO3*", Nature **429**, 850–853 (2004).

[6] C. D. Stanciu, F. Hansteen, A. V. Kimel, A. Kirilyuk, A. Tsukamoto, A. Itoh, and T. Rasing, "*All-Optical Magnetic Recording with Circularly Polarized Light*", Physical Review Letters **99**, 047601 (2007).

[7] I. Radu, K. Vahaplar, C. Stamm, T. Kachel, N. Pontius, H. A. Dürr, T. A. Ostler, J. Barker, R. F. L. Evans, R. W. Chantrell, A. Tsukamoto, A. Itoh, A. Kirilyuk, T. Rasing, and A. V. Kimel, "*Transient ferromagnetic-like state mediating ultrafast reversal of antiferromagnetically coupled spins*", Nature **472**, 205–208 (2011).

[8] A. Kirilyuk, A. V. Kimel, and T. Rasing, "*Laser-induced magnetization dynamics and reversal in ferrimagnetic alloys*", Reports on Progress in Physics **76**, 026501 (2013).

[9] S. Mangin, M. Gottwald, C. H. Lambert, D. Steil, V. Uhlíř, L. Pang, M. Hehn, S. Alebrand, M. Cinchetti, G. Malinowski, Y. Fainman, M. Aeschlimann, and E. E. Fullerton, "*Engineered materials for all-optical helicity-dependent magnetic switching*", Nature Materials **13**, 286–292 (2014).

[10] C.-H. Lambert, S. Mangin, B. S. D. C. S. Varaprasad, Y. K. Takahashi, M. Hehn, M. Cinchetti, G. Malinowski, K. Hono, Y. Fainman, M. Aeschlimann, and E. E. Fullerton, "*All-optical control of ferromagnetic thin films and nanostructures*", Science **345**, 1337–1340 (2014).

[11] T. Satoh, Y. Terui, R. Moriya, B. A. Ivanov, K. Ando, E. Saitoh, T. Shimura, and K. Kuroda, "*Directional control of spin-wave emission by spatially shaped light*", Nature Photonics **6**, 662–666 (2012).

[12] Y. Au, M. Dvornik, T. Davison, E. Ahmad, P. S. Keatley, A. Vansteenkiste, B. Van Waeyenberge, and V. V. Kruglyak, "*Direct Excitation of Propagating Spin Waves by Focused Ultrashort Optical Pulses*", Physical Review Letters **110**, 097201 (2013).

[13] S.-J. Yun, C.-G. Cho, and S.-B. Choe, "*Simultaneous excitation of two different spinwave modes by optical ultrafast demagnetization*", Applied Physics Express **8**, 063009 (2015).

[14] S. Iihama, Y. Sasaki, A. Sugihara, A. Kamimaki, Y. Ando, and S. Mizukami, "*Quantification of a propagating spin-wave-packet created by an ultrashort laser pulse in a thin film of magnetic metal*", Physical Review B **94**, 020401 (2016).

[15] M. Jäckl, V. Belotelov, I. Akimov, I. Savochkin, D. Yakovlev, A. Zvezdin, and M. Bayer, "*Magnon Accumulation by Clocked Laser Excitation as Source of Long-Range Spin Waves in Transparent Magnetic Films*", Physical Review X **7**, 021009 (2017).

[16] I. V. Savochkin, M. Jäckl, V. I. Belotelov, I. A. Akimov, M. A. Kozhaev, D. A. Sylgacheva, A. I. Chernov, A. N. Shaposhnikov, A. R. Prokopov, V. N. Berzhansky, D. R. Yakovlev, A. K. Zvezdin, and M. Bayer, "*Generation of spin waves by a train of fs-laser pulses: a novel approach for tuning magnon wavelength*", Scientific Reports **7**, 5668 (2017).

[17] S. Muralidhar, A. A. Awad, A. Alemán, R. Khymyn, M. Dvornik, D. Hanstorp, and J. Åkerman, "*Sustained coherent spin wave emission using frequency combs*", Physical Review B **101**, 224423 (2020).

[18] T. Kampfrath, M. Battiato, P. Maldonado, G. Eilers, J. Nötzold, S. Mährlein, V. Zbarsky, F. Freimuth, Y. Mokrousov, S. Blügel, M. Wolf, I. Radu, P. M. Oppeneer, and M. Münzenberg, "*Terahertz spin current pulses controlled by magnetic heterostructures*", Nature Nanotechnology **8**, 256–260 (2013).

[19] T. J. Huisman, R. V. Mikhaylovskiy, J. D. Costa, F. Freimuth, E. Paz, J. Ventura, P. P. Freitas, S. Blügel, Y. Mokrousov, T. Rasing, and A. V. Kimel, "*Femtosecond control of electric currents in metallic ferromagnetic heterostructures*", Nature Nanotechnology **11**, 455–458 (2016).

[20] T. Seifert, S. Jaiswal, U. Martens, J. Hannegan, L. Braun, P. Maldonado, F. Freimuth, A. Kronenberg, J. Henrizi, I. Radu, E. Beaurepaire, Y. Mokrousov, P. M. Oppeneer, M. Jourdan, G. Jakob, D. Turchinovich, L. M. Hayden, M. Wolf, M. Münzenberg, M. Kläui, and T. Kampfrath, "*Efficient metallic spintronic emitters of ultrabroadband terahertz radiation*", Nature Photonics **10**, 483–488 (2016).

[21] P. Němec, E. Rozkotová, N. Tesařová, F. Trojánek, E. De Ranieri, K. Olejník, J. Zemen, V. Novák, M. Cukr, P. Malý, and T. Jungwirth, "*Experimental observation of the optical spin transfer torque*", Nature Physics **8**, 411–415 (2012).

[22] M. Battiato, K. Carva, and P. M. Oppeneer, "*Superdiffusive spin transport as a mechanism of ultrafast demagnetization*", Physical Review Letters **105** (2010).

[23] A. J. Schellekens, K. C. Kuiper, R. R. De Wit, and B. Koopmans, "*Ultrafast spin-transfer torque driven by femtosecond pulsed-laser excitation*", Nature Communications **5** (2014).

[24] P. Baláž, M. Žonda, K. Carva, P. Maldonado, and P. M. Oppeneer, "*Transport theory for femtosecond laser-induced spin-transfer torques*", Journal of Physics Condensed Matter **30** (2018).

[25] M. L. Lalieu, R. Lavrijsen, and B. Koopmans, "*Integrating all-optical switching with spintronics*", Nature Communications **10**, 1–6 (2019).

[26] G. Ju, J. Hohlfeld, B. Bergman, R. J. Van Deveerdonk, O. N. Mryasov, J. Y. Kim, X. Wu, D. Weller, and B. Koopmans, "*Ultrafast generation of ferromagnetic order via a laser-induced phase transformation in FeRh thin films*", Physical Review Letters **93** (2004).

[27] J.-U. Thiele, M. Buess, and C. H. Back, "*Spin dynamics of the antiferromagnetic-to-ferromagnetic phase transition in FeRh on a sub-picosecond time scale*", Applied Physics Letters **85**, 2857–2859 (2004).

[28] S. Neusser and D. Grundler, "*Magnonics: Spin Waves on the Nanoscale*", Advance Materials **21**, 2927–2932 (2009).

[29] V. Kruglyak, S. Demokritov, and D. Grundler, "*Magnonics*", Journal of Physics D: Applied Physics **43**, 264001 (2010).

[30] S. O. Demokritov and A. N. Slavin, *Magnonics: From fundamentals to applications*, Topics in Applied Physics (Springer Nature, 2013).

[31] A. V. Chumak, V. I. Vasyuchka, A. A. Serga, and B. Hillebrands, "*Magnon spintronics*", Nature Physics **11**, 453–461 (2015).

[32] P. Wolf, "*Free Oscillations of the Magnetization in Permalloy Films*", Journal of Applied Physics **32**, S95–S96 (1961).

[33] A. K. Ganguly and D. C. Webb, "*Microstrip Excitation of Magnetostatic Surface Waves: Theory and Experiment*", IEEE Transactions on Microwave Theory and Technology **23**, 998–1006 (1975).

[34] V. E. Demidov, S. O. Demokritov, K. Rott, P. Krzysteczko, and G. Reiss, "*Nano-optics with spin waves at microwave frequencies*", Applied Physics Letters **92**, 232503 (2008).

[35] V. E. Demidov, S. Urazhdin, and S. O. Demokritov, "*Direct observation and mapping of spin waves emitted by spin-torque nano-oscillators*", Nature Materials **9**, 984–988 (2010).

[36] S. Bonetti, V. Tiberkevich, G. Consolo, G. Finocchio, P. Muduli, F. Mancoff, A. Slavin, and J. Åkerman, "*Experimental Evidence of Self-Localized and Propagating Spin Wave Modes in Obliquely Magnetized Current-Driven Nanocontacts*", Physical Review Letters **105**, 217204 (2010).

[37] M. Madami, S. Bonetti, G. Consolo, S. Tacchi, G. Carlotti, G. Gubbiotti, F. B. Mancoff, Y. M. A., and J. Åkerman, "*Direct observation of a propagating spin wave induced by spin-transfer torque*", Nature Nanotechnology **6**, 635–638 (2011).

[38] T. Chen, R. K. Dumas, A. Eklund, P. K. Muduli, A. Houshang, A. A. Awad, P. Dürrenfeld, B. G. Malm, A. Rusu, and J. Åkerman, "*Spin-torque and spin-Hall nano-oscillators*", Proceedings of the IEEE **104**, 1919–1945 (2016).

[39] A. Houshang, E. Iacocca, P. Dürrenfeld, S. Sani, J. Åkerman, and R. Dumas, "*Spin-wave-beam driven synchronization of nanocontact spin-torque oscillators*", Nature Nanotechnology **11**, 280 (2016).

[40] P. Dürrenfeld, A. A. Awad, A. Houshang, R. K. Dumas, and J. Åkerman, "*A 20 nm spin Hall nano-oscillator*", Nanoscale **9**, 1285–1291 (2017).

[41] A. Houshang, R. Khymyn, H. Fulara, A. Gangwar, M. Haidar, S. R. Etesami, R. Ferreira, P. P. Freitas, M. Dvornik, R. K. Dumas, and J. Åkerman, "*Spin transfer torque driven higher-order propagating spin waves in nano-contact magnetic tunnel junctions*", Nature Communications **9**, 4374 (2018).

[42] B. Divinskiy, V. E. Demidov, S. Urazhdin, R. Freeman, A. B. Rinkevich, and S. O. Demokritov, "*Excitation and Amplification of Spin Waves by Spin–Orbit Torque*", Advance Materials (2018) `10.1002/adma.201802837`.

[43] H. Fulara, M. Zahedinejad, R. Khymyn, A. A. Awad, S. Muralidhar, M. Dvornik, and J. Åkerman, "*Spin-orbit torque–driven propagating spin waves*", Science Advances **5** (2019).

[44] A. Kamimaki, S. Iihama, Y. Sasaki, Y. Ando, and S. Mizukami, "*Reciprocal excitation of propagating spin waves by a laser pulse and their reciprocal mapping in magnetic metal films*", Phys. Rev. B **96**, 014438 (2017).

[45] A. V. Kimel, A. Kirilyuk, P. A. Usachev, R. V. Pisarev, A. M. Balbashov, and T. Rasing, "*Ultrafast non-thermal control of magnetization by instantaneous photomagnetic pulses.*", Nature **435**, 655–7 (2005).

[46] M. Deb, M. Vomir, J. L. Rehspringer, and J. Y. Bigot, "*Ultrafast optical control of magnetization dynamics in polycrystalline bismuth doped iron garnet thin films*", Applied Physics Letters **107**, 252404 (2015).

[47] D. Bossini, S. Dal Conte, Y. Hashimoto, A. Secchi, R. V. Pisarev, T. Rasing, G. Cerullo, and A. V. Kimel, "*Macrospin dynamics in antiferromagnets triggered by sub-20 femtosecond injection of nanomagnons*", Nature Communications **7**, 10645 (2016).

[48] F. Hansteen, A. Kimel, A. Kirilyuk, and T. Rasing, "*Nonthermal ultrafast optical control of the magnetization in garnet films*", Physical Review B **73**, 014421 (2006).

[49] C. Berk, F. Ganss, M. Jaris, M. Albrecht, and H. Schmidt, "*All-Optical Multi-Pulse Pump-Probe Method for Selective Control of Magnetization Precessions in Magnetic Multilayers*", IEEE J. Quantum Electron., 1–1 (2019).

[50] L. Berger, "*Emission of spin waves by a magnetic multilayer traversed by a current*", Physical Review B **54**, 9353–9358 (1996).

[51] J. C. Slonczewski, "*Current-driven excitation of magnetic multilayers*", Journal of Magnetism and Magnetic Materials **159**, L1–L7 (1996).

[52] J. Slonczewski, "*Excitation of spin waves by an electric current*", Journal of Magnetism and Magnetic Materials **195**, L261–L268 (1999).

[53] S. Bonetti, V. Puliafito, G. Consolo, V. S. Tiberkevich, A. N. Slavin, and J. Åkerman, "*Power and linewidth of propagating and localized modes in nanocontact spin-torque oscillators*", Physical Review B **85**, 174427 (2012).

[54] A. Slavin and V. Tiberkevich, "*Spin Wave Mode Excited by Spin-Polarized Current in a Magnetic Nanocontact is a Standing Self-Localized Wave Bullet*", Physical Review Letters **95**, 237201 (2005).

[55] G. Gerhart, E. Bankowski, G. A. Melkov, V. S. Tiberkevich, and A. N. Slavin, "*Angular dependence of the microwave-generation threshold in a nanoscale spin-torque oscillator*", Physical Review B **76**, 024437 (2007).

[56] R. K. Dumas, E. Iacocca, S. Bonetti, S. R. Sani, S. M. Mohseni, A. Eklund, J. Persson, O. Heinonen, and J. Åkerman, "*Spin-Wave-Mode Coexistence on the Nanoscale: A Consequence of the Oersted-Field-Induced Asymmetric Energy Landscape*", Physical Review Letters **110**, 257202 (2013).

[57] M. A. Hoefer, T. J. Silva, and M. W. Keller, "*Theory for a dissipative droplet soliton excited by a spin torque nanocontact*", Physical Review B **82**, 054432 (2010).

[58] S. M. Mohseni, S. R. Sani, J. Persson, T. N. A. Nguyen, S. Chung, Y. Pogoryelov, P. K. Muduli, E. Iacocca, A. Eklund, R. K. Dumas, S. Bonetti, A. Deac, M. A. Hoefer, and J. Åkerman, "*Spin Torque–Generated Magnetic Droplet Solitons*", Science **339**, 1295–1298 (2013).

[59] F. Macià, D. Backes, and A. D. Kent, "*Stable magnetic droplet solitons in spin-transfer nanocontacts*", Nature Nanotechnology **9**, 992–996 (2014).

[60] S. Chung, Q. T. Le, M. Ahlberg, A. A. Awad, M. Weigand, I. Bykova, R. Khymyn, M. Dvornik, H. Mazraati, A. Houshang, S. Jiang, T. N. A. Nguyen, E. Goering, G. Schütz, J. Gräfe, and J. Åkerman, "*Direct Observation of Zhang-Li Torque Expansion of Magnetic Droplet Solitons*", Physical Review Letters **120**, 217204 (2018).

[61] V. E. Demidov, S. Urazhdin, H. Ulrichs, V. Tiberkevich, A. Slavin, D. Baither, G. Schmitz, and S. O. Demokritov, "*Magnetic nano-oscillator driven by pure spin current*", Nature Materials **11**, 1028 (2012).

[62] V. Demidov, S. Urazhdin, A. Zholud, A. Sadovnikov, and S. Demokritov, "*Nanoconstriction-based spin-Hall nano-oscillator*", Applied Physics Letters **105**, 172410 (2014).

[63] A. Awad, P. Dürrenfeld, A. Houshang, M. Dvornik, E. Iacocca, R. Dumas, and J. Åkerman, "*Long-range mutual synchronization of spin Hall nano-oscillators*", Nature Physics **13**, 292 (2017).

[64] M. Romera, P. Talatchian, S. Tsunegi, F. A. Araujo, V. Cros, P. Bortolotti, J. Trastoy, K. Yakushiji, A. Fukushima, H. Kubota, et al., "*Vowel recognition with four coupled spin-torque nano-oscillators*", Nature **563**, 230 (2018).

[65] L. D. Landau, *Collected papers of LD Landau* (Pergamon, 1965).

[66] T. L. Gilbert, "*A phenomenological theory of damping in ferromagnetic materials*", IEEE Transactions on Magnetics **40**, 3443–3449 (2004).

[67] F. Bloch, "*Zur Theorie des Ferromagnetismus*", Zeitschrift für Physik **61**, 206–219 (1930).

[68] T. Holstein and H. Primakoff, "*Field Dependence of the Intrinsic Domain Magnetization of a Ferromagnet*", Physical Review **58**, 1098–1113 (1940).

[69] L. Liu, C.-F. Pai, Y. Li, H. Tseng, D. Ralph, and R. Buhrman, "*Spin-torque switching with the giant spin Hall effect of tantalum*", Science **336**, 555–558 (2012).

[70] L. Liu, C.-F. Pai, D. Ralph, and R. Buhrman, "*Magnetic oscillations driven by the spin Hall effect in 3-terminal magnetic tunnel junction devices*", Physical Review Letters **109**, 186602 (2012).

[71] M. Ranjbar, P. Dürrenfeld, M. Haidar, E. Iacocca, M. Balinskiy, T. Le, M. Fazlali, A. Houshang, A. Awad, R. Dumas, and J. Åkerman, "*CoFeB-Based Spin Hall Nano-Oscillators*", IEEE Magnetics Letters **5**, 3000504 (2014).

[72] Z. Duan, A. Smith, L. Yang, B. Youngblood, J. Lindner, V. E. Demidov, S. O. Demokritov, and I. N. Krivorotov, "*Nanowire spin torque oscillator driven by spin orbit torques*", Nature Communications **5**, 5616 (2014).

[73] M. D'yakonov and V. Perel, "*Possibility of orienting electron spins with current*", Soviet Journal of Experimental and Theoretical Physics Letters **13**, 467 (1971).

[74] M. Dyakonov and V. Perel, "*Current-induced spin orientation of electrons in semiconductors*", Physics Letters A **35**, 459–460 (1971).

[75] A. Bakun, B. Zakharchenya, A. Rogachev, M. Tkachuk, and V. Fleisher, "*Detection of a surface photocurrent due to electron optical orientation in a semiconductor*", Sov. Phys. JETP Lett **40**, 1293 (1984).

[76] J. Hirsch, "*Spin hall effect*", Physical Review Letters **83**, 1834 (1999).

[77] J.-C. Rojas-Sánchez, N. Reyren, P. Laczkowski, W. Savero, J.-P. Attané, C. Deranlot, M. Jamet, J.-M. George, L. Vila, and H. Jaffrès, "*Spin pumping and inverse spin Hall effect in platinum: the essential role of spin-memory loss at metallic interfaces*", Physical Review Letters **112**, 106602 (2014).

[78] Y. Liu, Z. Yuan, R. J. Wesselink, A. A. Starikov, and P. J. Kelly, "*Interface enhancement of Gilbert damping from first principles*", Physical Review Letters **113**, 207202 (2014).

[79] W. Zhang, W. Han, X. Jiang, S.-H. Yang, and S. S. Parkin, "*Role of transparency of platinum–ferromagnet interfaces in determining the intrinsic magnitude of the spin Hall effect*", Nature Physics **11**, 496 (2015).

[80] C.-F. Pai, Y. Ou, L. H. Vilela-Leão, D. Ralph, and R. Buhrman, "*Dependence of the efficiency of spin Hall torque on the transparency of Pt/ferromagnetic layer interfaces*", Physical Review B **92**, 064426 (2015).

[81] M. Dvornik, A. A. Awad, and J. Åkerman, "*Origin of Magnetization Auto-Oscillations in Constriction-Based Spin Hall Nano-Oscillators*", Physical Review Applied **9**, 014017 (2018).

[82] B. Koopmans, G. Malinowski, F. Dalla Longa, D. Steiauf, M. Fähnle, T. Roth, M. Cinchetti, and M. Aeschlimann, "*Explaining the paradoxical diversity of ultrafast laser-induced demagnetization*", Nature Materials **9**, 259–265 (2010).

[83] P. Dürrenfeld, *Spin torque and spin Hall nano-oscillators with single magnetic layers* (2015).

[84] A. Houshang, "*Synchronization Phenomena in Spin Torque and Spin Hall Nano-Oscillators*", (2017).

[85] M. Zahedinejad, "*Spin Hall Nano-Oscillator Arrays: Towards GHz Neuromorphics*", (2019).

[86] H. Mazraati, M. Zahedinejad, and J. Åkerman, "*Improving the magnetodynamical properties of NiFe/Pt bilayers through Hf dusting*", Applied Physics Letters **113**, 092401 (2018).

[87] H. Yu, O. d' Allivy Kelly, V. Cros, R. Bernard, P. Bortolotti, A. Anane, F. Brandl, F. Heimbach, and D. Grundler, "*Approaching soft X-ray wavelengths in nanomagnet-based microwave technology*", Nature Communications **7**, 11255 (2016).

[88] B. Koopmans, G. Malinowski, F. Dalla Longa, D. Steiauf, M. Fähnle, T. Roth, M. Cinchetti, and M. Aeschlimann, "*Explaining the paradoxical diversity of ultrafast laser-induced demagnetization*", Nature Materials **9**, 259–265 (2010).

[89] D. Rudolf, C. La-O-Vorakiat, M. Battiato, R. Adam, J. M. Shaw, E. Turgut, P. Maldonado, S. Mathias, P. Grychtol, H. T. Nembach, T. J. Silva, M. Aeschlimann, H. C. Kapteyn, M. M. Murnane, C. M. Schneider, and P. M. Oppeneer, "*Ultrafast magnetization enhancement in metallic multilayers driven by superdiffusive spin current*", Nature Communications **3**, 1037 (2012).

[90] Q. Zhang, A. V. Nurmikko, A. Anguelouch, G. Xiao, and A. Gupta, "*Coherent Magnetization Rotation and Phase Control by Ultrashort Optical Pulses in* CrO_2 *Thin Films*", Physical Review Letters **89**, 177402 (2002).

[91] M. Vomir, L. H. F. Andrade, L. Guidoni, E. Beaurepaire, and J.-Y. Bigot, "*Real Space Trajectory of the Ultrafast Magnetization Dynamics in Ferromagnetic Metals*", Physical Review Letters **94**, 237601 (2005).

[92] V. V. Kruglyak, A. Barman, R. J. Hicken, J. R. Childress, and J. A. Katine, "*Picosecond magnetization dynamics in nanomagnets: Crossover to nonuniform precession*", Physical Review B **71**, 220409 (2005).

[93] A. V. Kimel, C. D. Stanciu, P. A. Usachev, R. V. Pisarev, V. N. Gridnev, A. Kirilyuk, and T. Rasing, "*Optical excitation of antiferromagnetic resonance in* $TmFeO_3$", Physical Review B **74**, 060403 (2006).

[94] V. E. Demidov, B. Hillebrands, S. O. Demokritov, M. Laufenberg, and P. P. Freitas, "*Two-dimensional patterns of spin-wave radiation by rectangular spin-valve elements*", Journal of Applied Physics **97**, 10A717 (2005).

[95] C. W. Sandweg, M. B. Jungfleisch, V. I. Vasyuchka, A. A. Serga, P. Clausen, H. Schultheiss, B. Hillebrands, A. Kreisel, and P. Kopietz, "*Wide-range wavevector selectivity of magnon gases in Brillouin light scattering spectroscopy*", Review of Scientific Instrument **81**, 73902 (2010).

[96] T. Sebastian, K. Schultheiss, B. Obry, B. Hillebrands, and H. Schultheiss, "*Micro-focused Brillouin light scattering: imaging spin waves at the nanoscale*", Frontiers in Physics **3**, 1–23 (2015).

[97] K. S. Olsson, K. An, and X. Li, "*Magnon and phonon thermometry with inelastic light scattering*", Journal of Physics D **51**, 133001 (2018).

[98] J. TrägÅrdh, K. Macrae, C. Travis, R. Amor, G. Norris, S. Wilson, G.-L. Oppo, and G. Mcconnell, "*A simple but precise method for quantitative measurement of the quality of the laser focus in a scanning optical microscope*", Journal of Microscopy **259**, 66–73 (2015).

[99] A. Vansteenkiste, J. Leliaert, M. Dvornik, M. Helsen, F. Garcia-Sanchez, and B. Van Waeyenberge, "*The design and verification of MuMax3*", AIP Advances **4**, 107133 (2014).

[100] O. Dzyapko, I. Lisenkov, P. Nowik-Boltyk, V. E. Demidov, S. O. Demokritov, B. Koene, A. Kirilyuk, T. Rasing, V. Tiberkevich, and A. Slavin, "*Magnon-magnon interactions in a room-temperature magnonic Bose-Einstein condensate*", Physical Review B **96**, 064438 (2017).

[101] O. Stavroudis, *The optics of rays, wavefronts, and caustics*, Vol. 38 (Elsevier, 2012).

[102] J. F. Nye, *Natural focusing and fine structure of light: caustics and wave dislocations* (CRC Press, 1999).

[103] P. Manogg, "*Anwendung der Schattenoptik zur Untersuchung des Zerreißvorgangs von Platten*", Dissertation University of Freiburg (1964).

[104] P. S. Theocaris, "*Local Yielding Around a Crack Tip in Plexiglas*", Journal of Applied Mechanics **37**, 409–415 (1970).

[105] P. S. Theocaris, "Elastic stress intensity factors evaluated by caustics", in *Experimental evaluation of stress concentration and intensity factors: Useful methods and solutions to Experimentalists in fracture mechanics*, edited by G. C. Sih (Springer Netherlands, Dordrecht, 1981), pp. 189–252.

[106] J. F. Kalthoff, "The Shadow Optical Method of Caustics", in *Static and Dynamic Photoelasticity and Caustics: Recent Developments*, edited by A. Lagarde (Springer Vienna, Vienna, 1987), pp. 407–522.

[107] B. Taylor, H. J. Maris, and C. Elbaum, "*Phonon Focusing in Solids*", Physical Review Letters **23**, 416–419 (1969).

[108] A. G. Every, "*Formation of phonon-focusing caustics in crystals*", Physical Review B **34**, 2852–2862 (1986).

[109] A. Maznev and A. Every, "*Formation of surface phonon focusing caustics in crystals*", Solid State Communications **97**, 679–687 (1996).

[110] C. J. Hogan, "*Gravitational Lensing by Cold Dark Matter Catastrophes*", The Astrophysical Journal **527**, 42–45 (1999).

[111] C. J. Hogan, "*Particle annihilation in cold dark matter micropancakes*", Physical Review D **64**, 063515 (2001).

[112] V. Veerakumar and R. E. Camley, "*Magnon focusing in thin ferromagnetic films*", Physical Review B **74**, 214401 (2006).

[113] V. Veerakumar and R. E. Camley, "*Focusing of spin waves in YIG thin films*", IEEE Transactions on Magnetics **42**, 3318–3320 (2006).

[114] V. Veerakumar and R. E. Camley, "*Magnetostatic bulk and surface spin-wave focusing in antiferromagnetic thin films*", Physical Review B **81**, 174432 (2010).

[115] M. Bauer, O. Büttner, S. O. Demokritov, B. Hillebrands, V. Grimalsky, Y. Rapoport, and A. N. Slavin, "*Observation of Spatiotemporal Self-Focusing of Spin Waves in Magnetic Films*", Physical Review Letters **81**, 3769–3772 (1998).

[116] O. Büttner, M. Bauer, S. O. Demokritov, B. Hillebrands, Y. S. Kivshar, V. Grimalsky, Y. Rapoport, and A. N. Slavin, "*Linear and nonlinear diffraction of dipolar spin waves in yttrium iron garnet films observed by space- and time-resolved Brillouin light scattering*", Physical Review B **61**, 11576–11587 (2000).

[117] T. Schneider, A. A. Serga, A. V. Chumak, C. W. Sandweg, S. Trudel, S. Wolff, M. P. Kostylev, V. S. Tiberkevich, A. N. Slavin, and B. Hillebrands, "*Nondiffractive Subwavelength Wave Beams in a Medium with Externally Controlled Anisotropy*", Physical Review Letters **104**, 197203 (2010).

[118] V. E. Demidov, S. O. Demokritov, D. Birt, B. O'Gorman, M. Tsoi, and X. Li, "*Radiation of spin waves from the open end of a microscopic magnetic-film waveguide*", Physical Review B **80**, 014429 (2009).

[119] F. Heussner, A. A. Serga, T. Brächer, B. Hillebrands, and P. Pirro, "*A switchable spin-wave signal splitter for magnonic networks*", Applied Physics Letters **111**, 122401 (2017).

[120] C. S. Davies, A. V. Sadovnikov, S. V. Grishin, Y. P. Sharaevskii, S. A. Nikitov, and V. V. Kruglyak, "*Generation of propagating spin waves from regions of increased dynamic demagnetising field near magnetic antidots*", Applied Physics Letters **107**, 162401 (2015).

[121] R. Gieniusz, H. Ulrichs, V. D. Bessonov, U. Guzowska, A. I. Stognii, and A. Maziewski, "*Single antidot as a passive way to create caustic spin-wave beams in yttrium iron garnet films*", Applied Physics Letters **102**, 102409 (2013).

[122] B. A. Kalinikos and A. N. Slavin, "*Theory of dipole-exchange spin wave spectrum for ferromagnetic films with mixed exchange boundary conditions*", Journal of Physics C: Solid State Physics **19**, 7013–7033 (1986).

[123] H. Mazraati, S. Chung, A. Houshang, M. Dvornik, L. Piazza, F. Qejvanaj, S. Jiang, T. Q. Le, J. Weissenrieder, and J. Åkerman, "*Low operational current spin Hall nano-oscillators based on NiFe/W bilayers*", Applied Physics Letters **109**, 242402 (2016).

[124] M. Zahedinejad, A. A. Awad, P. Dürrenfeld, A. Houshang, Y. Yin, P. K. Muduli, and J. Åkerman, "*Current Modulation of Nanoconstriction Spin-Hall Nano-Oscillators*", IEEE Magnetics Letters **8**, 1–4 (2017).

[125] H. Mazraati, S. R. Etesami, S. A. H. Banuazizi, S. Chung, A. Houshang, A. A. Awad, M. Dvornik, and J. Åkerman, "*Auto-oscillating Spin-Wave Modes of Constriction-Based Spin Hall Nano-oscillators in Weak In-Plane Fields*", Physical Review Applied **10**, 054017 (2018).

[126] M. Zahedinejad, H. Mazraati, H. Fulara, J. Yue, S. Jiang, A. A. Awad, and J. Åkerman, "*CMOS compatible W/CoFeB/MgO spin Hall nano-oscillators with wide frequency tunability*", Applied Physics Letters **112**, 132404 (2018).

[127] T. M. Spicer, P. S. Keatley, M. Dvornik, T. H. J. Loughran, A. A. Awad, P. Dürrenfeld, A. Houshang, M. Ranjbar, J. Åkerman, V. V. Kruglyak, and R. J. Hicken, "*Time resolved imaging of the non-linear bullet mode within an injection-locked nano-contact spin Hall nano-oscillator*", Applied Physics Letters **113**, 192405 (2018).

[128] T. M. Spicer, P. S. Keatley, T. H. J. Loughran, M. Dvornik, A. A. Awad, P. Dürrenfeld, A. Houshang, M. Ranjbar, J. Åkerman, V. V. Kruglyak, and R. J. Hicken, "*Spatial mapping of torques within a spin Hall nano-oscillator*", Physical Review B **98**, 214438 (2018).

[129] M. Haidar, A. A. Awad, M. Dvornik, R. Khymyn, A. Houshang, and J. Åkerman, "*A single layer spin-orbit torque nano-oscillator*", Nature Communications **10**, 2362 (2019).

[130] A. A. Awad, A. Houshang, M. Zahedinejad, R. Khymyn, and J. Åkerman, "*Width dependent auto-oscillating properties of constriction based spin Hall nano-oscillators*", Applied Physics Letters **116**, 232401 (2020).

[131] Y. Zhou and J. Åkerman, "*Perpendicular spin torque promotes synchronization of magnetic tunnel junction based spin torque oscillators*", Applied Physics Letters **94**, 112503 (2009).

[132] R. K. Dumas, S. R. Sani, S. M. Mohseni, E. Iacocca, Y. Pogoryelov, P. K. Muduli, S. Chung, P. Dürrenfeld, and J. Åkerman, "*Recent advances in nanocontact spin-torque oscillators*", IEEE Transactions on Magnetics **50**, 1–7 (2014).

[133] S. Sani, J. Persson, S. M. Mohseni, Y. Pogoryelov, P. K. Muduli, A. Eklund, G. Malm, M. Käll, A. Dmitriev, and J. Åkerman, "*Mutually synchronized bottom-up multi-nanocontact spin–torque oscillators*", Nature Communications **4**, 2731 (2013).

[134] T. Kendziorczyk, S. O. Demokritov, and T. Kuhn, "*Spin-wave-mediated mutual synchronization of spin-torque nano-oscillators: A micromagnetic study of multistable phase locking*", Physical Review B **90**, 054414 (2014).

[135] M. Madami, E. Iacocca, S. Sani, G. Gubbiotti, S. Tacchi, R. K. Dumas, J. Åkerman, and G. Carlotti, "*Propagating spin waves excited by spin-transfer torque: A combined electrical and optical study*", Physical Review B **92**, 024403 (2015).

[136] Y. Penn, M. Segal, and E. Moses, "*Network synchronization in hippocampal neurons*", Proceedings of the National Academy of Sciences **113**, 3341–3346 (2016).

[137] J. Veit, R. Hakim, M. P. Jadi, T. J. Sejnowski, and H. Adesnik, "*Cortical gamma band synchronization through somatostatin interneurons*", Nature Neuroscience **20**, 951 (2017).

[138] J. Buck, "*Synchronous rhythmic flashing of fireflies. II.*", The Quarterly review of biology **63**, 265–289 (1988).

[139] Y. Fang, V. V. Yashin, S. P. Levitan, and A. C. Balazs, "*Pattern recognition with "materials that compute"*", Science advances **2**, e1601114 (2016).

[140] K. Segall, M. LeGro, S. Kaplan, O. Svitelskiy, S. Khadka, P. Crotty, and D. Schult, "*Synchronization dynamics on the picosecond time scale in coupled Josephson junction neurons*", Physical Review E **95**, 032220 (2017).

[141] M. A. Galin, E. A. Borodianskyi, V. Kurin, I. Shereshevskiy, N. Vdovicheva, V. M. Krasnov, and A. Klushin, "*Synchronization of Large Josephson-Junction Arrays by Traveling Electromagnetic Waves*", Physical Review Applied **9**, 054032 (2018).

[142] Y. Li, X. De Milly, O. Klein, V. Cros, J. Grollier, and G. De Loubens, "*Selective control of vortex polarities by microwave field in two robustly synchronized spin-torque nano-oscillators*", Applied Physics Letters **112**, 022405 (2018).

[143] S. Tsunegi, T. Taniguchi, R. Lebrun, K. Yakushiji, V. Cros, J. Grollier, A. Fukushima, S. Yuasa, and H. Kubota, "*Scaling up electrically synchronized spin torque oscillator networks*", Scientific Reports **8**, 13475 (2018).

[144] M. Zahedinejad, A. A. Awad, S. Muralidhar, R. Khymyn, H. Fulara, H. Mazraati, M. Dvornik, and J. Åkerman, "*Two-dimensional mutually synchronized spin Hall nano-oscillator arrays for neuromorphic computing*", en, Nature Nanotechnology **15**, 47–52 (2020).

[145] F. C. Hoppensteadt and E. M. Izhikevich, "*Oscillatory Neurocomputers with Dynamic Connectivity*", Physical Review Letters **82**, 2983–2986 (1999).

[146] T. Aonishi, K. Kurata, and M. Okada, "*Statistical Mechanics of an Oscillator Associative Memory with Scattered Natural Frequencies*", Physical Review Letters **82**, 2800–2803 (1999).

[147] H. Jaeger and H. Haas, "*Harnessing Nonlinearity: Predicting Chaotic Systems and Saving Energy in Wireless Communication*", Science **304**, 78–80 (2004).

[148] M. D. Pickett, G. Medeiros-Ribeiro, and R. S. Williams, "*A scalable neuristor built with Mott memristors*", Nature Materials **12**, 114–117 (2013).

[149] K. Segall, M. LeGro, S. Kaplan, O. Svitelskiy, S. Khadka, P. Crotty, and D. Schult, "*Synchronization dynamics on the picosecond time scale in coupled Josephson junction neurons*", Physical Review E **95**, 032220 (2017).

[150] J. Torrejon, M. Riou, F. A. Araujo, S. Tsunegi, G. Khalsa, D. Querlioz, P. Bortolotti, V. Cros, K. Yakushiji, A. Fukushima, H. Kubota, S. Yuasa, M. D. Stiles, and J. Grollier, "*Neuromorphic computing with nanoscale spintronic oscillators*", Nature **547**, 428–431 (2017).

[151] A. Parihar, N. Shukla, M. Jerry, S. Datta, and A. Raychowdhury, "*Vertex coloring of graphs via phase dynamics of coupled oscillatory networks*", Scientific Reports **7**, 911 (2017).

[152] A. Velichko, M. Belyaev, and P. Boriskov, "*A Model of an Oscillatory Neural Network with Multilevel Neurons for Pattern Recognition and Computing*", Electronics **8**, 75 (2019).

[153] T. Zhang, M. Haider, Y. Massoud, and J. Alexander, "*An Oscillatory Neural Network Based Local Processing Unit for Pattern Recognition Applications*", Electronics **8**, 64 (2019).

[154] A. Kumar and P. Mohanty, "*Autoassociative memory and pattern recognition in micromechanical oscillator network*", Scientific Reports **7**, 411 (2017).

[155] D. E. Nikonov, G. Csaba, W. Porod, T. Shibata, D. Voils, D. Hammerstrom, I. A. Young, and G. I. Bourianoff, "*Coupled-oscillator associative memory array operation for pattern recognition*", IEEE Journal on Exploratory Solid-State Computational Devices and Circuits **1**, 85–93 (2015).

[156] A. Novikov and E. Benderskaya, "*Oscillatory network based on Kuramoto model for image segmentation*", in International Conference on Parallel Computing Technologies (Springer, 2015), pp. 210–221.

[157] T. Raiko and H. Valpola, "*Oscillatory neural network for image segmentation with biased competition for attention*", in *From brains to systems* (Springer, 2011), pp. 75–85.

[158] T. Wang, L. Wu, and J. Roychowdhury, "*New Computational Results and Hardware Prototypes for Oscillator-based Ising Machines*", in Proceedings of the 56th Annual Design Automation Conference 2019 (ACM, 2019), p. 239.

[159] T. Wang and J. Roychowdhury, "*OIM: Oscillator-Based Ising Machines for Solving Combinatorial Optimisation Problems*", in Unconventional Computation and Natural Computation, edited by I. McQuillan and S. Seki (2019), pp. 232–256.

[160] I. Mahboob, H. Okamoto, and H. Yamaguchi, "*An electromechanical Ising Hamiltonian*", Science advances **2**, e1600236 (2016).

[161] E. Farhi, J. Goldstone, S. Gutmann, J. Lapan, A. Lundgren, and D. Preda, "*A Quantum Adiabatic Evolution Algorithm Applied to Random Instances of an NP-Complete Problem*", Science **292**, 472–475 (2001).

[162] S. Boixo, T. F. Rønnow, S. V. Isakov, Z. Wang, D. Wecker, D. A. Lidar, J. M. Martinis, and M. Troyer, "*Evidence for quantum annealing with more than one hundred qubits*", Nature Physics **10**, 218–224 (2014).

[163] S. Tsukamoto, M. Takatsu, S. Matsubara, and H. Tamura, "*An accelerator architecture for combinatorial optimization problems*", Fujitsu Scientific and Technical Journal **53**, 8–13 (2017).

[164] B. Sutton, K. Y. Camsari, B. Behin-Aein, and S. Datta, "*Intrinsic optimization using stochastic nanomagnets*", Scientific Reports **7**, 44370– (2017).

[165] J. Chou, S. Bramhavar, S. Ghosh, and W. Herzog, "*Analog Coupled Oscillator Based Weighted Ising Machine*", Scientific Reports **9**, 1–10 (2019).

[166] C. Roques-carmes, Y. Shen, L. Jing, T. Dubcek, S. Skirlo, H. Bagherianlemraski, and M. Soljacic, "*Optical Ising Machines and Optical Convolutional Neural Networks*", 20190019100 (Jan. 2019).

[167] Y. Yamamoto, K. Aihara, T. Leleu, K.-i. Kawarabayashi, S. Kako, M. Fejer, K. Inoue, and H. Takesue, "*Coherent Ising machines: optical neural networks operating at the quantum limit*", NPJ Quantum Information **3**, 49 (2017).

[168] R. Hamerly, T. Inagaki, P. L. McMahon, D. Venturelli, A. Marandi, T. Onodera, E. Ng, C. Langrock, K. Inaba, T. Honjo, et al., "*Experimental investigation of performance differences between coherent Ising machines and a quantum annealer*", Science Advances **5** (2019).

[169] T. Inagaki, Y. Haribara, K. Igarashi, T. Sonobe, S. Tamate, T. Honjo, A. Marandi, P. L. McMahon, T. Umeki, K. Enbutsu, et al., "*A coherent Ising machine for 2000-node optimization problems*", Science **354**, 603–606 (2016).

[170] A. Marandi, Z. Wang, K. Takata, R. L. Byer, and Y. Yamamoto, "*Network of time-multiplexed optical parametric oscillators as a coherent Ising machine*", Nature Photonics **8**, 937 (2014).

[171] T. Wang and J. Roychowdhury, "*OIM: Oscillator-based Ising Machines for Solving Combinatorial Optimisation Problems*", in International Conference on Unconventional Computation and Natural Computation (Springer, 2019), pp. 232–256.

[172] T. Wang, L. Wu, and J. Roychowdhury, "*New computational results and hardware prototypes for oscillator-based Ising machines*", in Proceedings of the 56th Annual Design Automation Conference 2019 (2019), pp. 1–2.